Measurements of $e^+e^- \to K^+K^-\eta$, $K^+K^-\pi^0$, and $K^0_S K^\pm\pi^\mp$ cross sections using initial state radiation events

B. Aubert,[1] M. Bona,[1] D. Boutigny,[1] Y. Karyotakis,[1] J. P. Lees,[1] V. Poireau,[1] X. Prudent,[1] V. Tisserand,[1] A. Zghiche,[1] J. Garra Tico,[2] E. Grauges,[2] L. Lopez,[3] A. Palano,[3] M. Pappagallo,[3] G. Eigen,[4] B. Stugu,[4] L. Sun,[4] G. S. Abrams,[5] M. Battaglia,[5] D. N. Brown,[5] J. Button-Shafer,[5] R. N. Cahn,[5] Y. Groysman,[5] R. G. Jacobsen,[5] J. A. Kadyk,[5] L. T. Kerth,[5] Yu. G. Kolomensky,[5] G. Kukartsev,[5] D. Lopes Pegna,[5] G. Lynch,[5] L. M. Mir,[5] T. J. Orimoto,[5] I. L. Osipenkov,[5] M. T. Ronan,[5,*] K. Tackmann,[5] T. Tanabe,[5] W. A. Wenzel,[5] P. del Amo Sanchez,[6] C. M. Hawkes,[6] A. T. Watson,[6] H. Koch,[7] T. Schroeder,[7] D. Walker,[8] D. J. Asgeirsson,[9] T. Cuhadar-Donszelmann,[9] B. G. Fulsom,[9] C. Hearty,[9] T. S. Mattison,[9] J. A. McKenna,[9] M. Barrett,[10] A. Khan,[10] M. Saleem,[10] L. Teodorescu,[10] V. E. Blinov,[11] A. D. Bukin,[11] V. P. Druzhinin,[11] V. B. Golubev,[11] A. P. Onuchin,[11] S. I. Serednyakov,[11] Yu. I. Skovpen,[11] E. P. Solodov,[11] K. Yu. Todyshev,[11] M. Bondioli,[12] S. Curry,[12] I. Eschrich,[12] D. Kirkby,[12] A. J. Lankford,[12] P. Lund,[12] M. Mandelkern,[12] E. C. Martin,[12] D. P. Stoker,[12] S. Abachi,[13] C. Buchanan,[13] J. W. Gary,[14] F. Liu,[14] O. Long,[14] B. C. Shen,[14,*] G. M. Vitug,[14] L. Zhang,[14] H. P. Paar,[15] S. Rahatlou,[15] V. Sharma,[15] J. W. Berryhill,[16] C. Campagnari,[16] A. Cunha,[16] B. Dahmes,[16] T. M. Hong,[16] D. Kovalskyi,[16] J. D. Richman,[16] T. W. Beck,[17] A. M. Eisner,[17] C. J. Flacco,[17] C. A. Heusch,[17] J. Kroseberg,[17] W. S. Lockman,[17] T. Schalk,[17] B. A. Schumm,[17] A. Seiden,[17] M. G. Wilson,[17] L. O. Winstrom,[17] E. Chen,[18] C. H. Cheng,[18] F. Fang,[18] D. G. Hitlin,[18] I. Narsky,[18] T. Piatenko,[18] F. C. Porter,[18] R. Andreassen,[19] G. Mancinelli,[19] B. T. Meadows,[19] K. Mishra,[19] M. D. Sokoloff,[19] F. Blanc,[20] P. C. Bloom,[20] S. Chen,[20] W. T. Ford,[20] J. F. Hirschauer,[20] A. Kreisel,[20] M. Nagel,[20] U. Nauenberg,[20] A. Olivas,[20] J. G. Smith,[20] K. A. Ulmer,[20] S. R. Wagner,[20] J. Zhang,[20] A. M. Gabareen,[21] A. Soffer,[21,+] W. H. Toki,[21] R. J. Wilson,[21] F. Winklmeier,[21] D. D. Altenburg,[22] E. Feltresi,[22] A. Hauke,[22] H. Jasper,[22] J. Merkel,[22] A. Petzold,[22] B. Spaan,[22] K. Wacker,[22] V. Klose,[23] M. J. Kobel,[23] H. M. Lacker,[23] W. F. Mader,[23] R. Nogowski,[23] J. Schubert,[23] K. R. Schubert,[23] R. Schwierz,[23] J. E. Sundermann,[23] A. Volk,[23] D. Bernard,[24] G. R. Bonneaud,[24] E. Latour,[24] V. Lombardo,[24] Ch. Thiebaux,[24] M. Verderi,[24] P. J. Clark,[25] W. Gradl,[25] F. Muheim,[25] S. Playfer,[25] A. I. Robertson,[25] J. E. Watson,[25] Y. Xie,[25] M. Andreotti,[26] D. Bettoni,[26] C. Bozzi,[26] R. Calabrese,[26] A. Cecchi,[26] G. Cibinetto,[26] P. Franchini,[26] E. Luppi,[26] M. Negrini,[26] A. Petrella,[26] L. Piemontese,[26] E. Prencipe,[26] V. Santoro,[26] F. Anulli,[27] R. Baldini-Ferroli,[27] A. Calcaterra,[27] R. de Sangro,[27] G. Finocchiaro,[27] S. Pacetti,[27] P. Patteri,[27] I. M. Peruzzi,[27,‡] M. Piccolo,[27] M. Rama,[27] A. Zallo,[27] A. Buzzo,[28] R. Contri,[28] M. Lo Vetere,[28] M. M. Macri,[28] M. R. Monge,[28] S. Passaggio,[28] C. Patrignani,[28] E. Robutti,[28] A. Santroni,[28] S. Tosi,[28] K. S. Chaisanguanthum,[29] M. Morii,[29] J. Wu,[29] R. S. Dubitzky,[30] J. Marks,[30] S. Schenk,[30] U. Uwer,[30] D. J. Bard,[31] P. D. Dauncey,[31] R. L. Flack,[31] J. A. Nash,[31] W. Panduro Vazquez,[31] M. Tibbetts,[31] P. K. Behera,[32] X. Chai,[32] M. J. Charles,[32] U. Mallik,[32] J. Cochran,[33] H. B. Crawley,[33] L. Dong,[33] V. Eyges,[33] W. T. Meyer,[33] S. Prell,[33] E. I. Rosenberg,[33] A. E. Rubin,[33] Y. Y. Gao,[34] A. V. Gritsan,[34] Z. J. Guo,[34] C. K. Lae,[34] A. G. Denig,[35] M. Fritsch,[35] G. Schott,[35] N. Arnaud,[36] J. Béquilleux,[36] A. D'Orazio,[36] M. Davier,[36] G. Grosdidier,[36] A. Höcker,[36] V. Lepeltier,[36] F. Le Diberder,[36] A. M. Lutz,[36] S. Pruvot,[36] S. Rodier,[36] P. Roudeau,[36] M. H. Schune,[36] J. Serrano,[36] V. Sordini,[36] A. Stocchi,[36] L. Wang,[36] W. F. Wang,[36] G. Wormser,[36] D. J. Lange,[37] D. M. Wright,[37] I. Bingham,[38] J. P. Burke,[38] C. A. Chavez,[38] J. R. Fry,[38] E. Gabathuler,[38] R. Gamet,[38] D. E. Hutchcroft,[38] D. J. Payne,[38] K. C. Schofield,[38] C. Touramanis,[38] A. J. Bevan,[39] K. A. George,[39] F. Di Lodovico,[39] R. Sacco,[39] G. Cowan,[40] H. U. Flaecher,[40] D. A. Hopkins,[40] S. Paramesvaran,[40] F. Salvatore,[40] A. C. Wren,[40] D. N. Brown,[41] C. L. Davis,[41] J. Allison,[42] N. R. Barlow,[42] R. J. Barlow,[42] Y. M. Chia,[42] C. L. Edgar,[42] G. D. Lafferty,[42] T. J. West,[42] J. I. Yi,[42] J. Anderson,[43] C. Chen,[43] A. Jawahery,[43] D. A. Roberts,[43] G. Simi,[43] J. M. Tuggle,[43] C. Dallapiccola,[44] S. S. Hertzbach,[44] X. Li,[44] T. B. Moore,[44] E. Salvati,[44] S. Saremi,[44] R. Cowan,[45] D. Dujmic,[45] P. H. Fisher,[45] K. Koeneke,[45] G. Sciolla,[45] M. Spitznagel,[45] F. Taylor,[45] R. K. Yamamoto,[45] M. Zhao,[45] Y. Zheng,[45] S. E. Mclachlin,[46,*] P. M. Patel,[46] S. H. Robertson,[46] A. Lazzaro,[47] F. Palombo,[47] J. M. Bauer,[48] L. Cremaldi,[48] V. Eschenburg,[48] R. Godang,[48] R. Kroeger,[48] D. A. Sanders,[48] D. J. Summers,[48] H. W. Zhao,[48] S. Brunet,[49] D. Côté,[49] M. Simard,[49] P. Taras,[49] F. B. Viaud,[49] H. Nicholson,[50] G. De Nardo,[51] F. Fabozzi,[51,§] L. Lista,[51] D. Monorchio,[51] C. Sciacca,[51] M. A. Baak,[52] G. Raven,[52] H. L. Snoek,[52] C. P. Jessop,[53] K. J. Knoepfel,[53] J. M. LoSecco,[53] G. Benelli,[54] L. A. Corwin,[54] K. Honscheid,[54] H. Kagan,[54] R. Kass,[54] J. P. Morris,[54] A. M. Rahimi,[54] J. J. Regensburger,[54] S. J. Sekula,[54] Q. K. Wong,[54] N. L. Blount,[55] J. Brau,[55] R. Frey,[55] O. Igonkina,[55] J. A. Kolb,[55] M. Lu,[55] R. Rahmat,[55] N. B. Sinev,[55] D. Strom,[55] J. Strube,[55] E. Torrence,[55] N. Gagliardi,[56] A. Gaz,[56] M. Margoni,[56] M. Morandin,[56] A. Pompili,[56] M. Posocco,[56] M. Rotondo,[56] F. Simonetto,[56] R. Stroili,[56] C. Voci,[56] E. Ben-Haim,[57] H. Briand,[57] G. Calderini,[57] J. Chauveau,[57] P. David,[57] L. Del Buono,[57] Ch. de la Vaissière,[57] O. Hamon,[57] Ph. Leruste,[57] J. Malclès,[57] J. Ocariz,[57] A. Perez,[57] J. Prendki,[57] L. Gladney,[58] M. Biasini,[59] R. Covarelli,[59] E. Manoni,[59] C. Angelini,[60] G. Batignani,[60]

S. Bettarini,[60] M. Carpinelli,[60,‖] R. Cenci,[60] A. Cervelli,[60] F. Forti,[60] M. A. Giorgi,[60] A. Lusiani,[60] G. Marchiori,[60] M. A. Mazur,[60] M. Morganti,[60] N. Neri,[60] E. Paoloni,[60] G. Rizzo,[60] J. J. Walsh,[60] J. Biesiada,[61] P. Elmer,[61] Y. P. Lau,[61] C. Lu,[61] J. Olsen,[61] A. J. S. Smith,[61] A. V. Telnov,[61] E. Baracchini,[62] F. Bellini,[62] G. Cavoto,[62] D. del Re,[62] E. Di Marco,[62] R. Faccini,[62] F. Ferrarotto,[62] F. Ferroni,[62] M. Gaspero,[62] P. D. Jackson,[62] M. A. Mazzoni,[62] S. Morganti,[62] G. Piredda,[62] F. Polci,[62] F. Renga,[62] C. Voena,[62] M. Ebert,[63] T. Hartmann,[63] H. Schröder,[63] R. Waldi,[63] T. Adye,[64] G. Castelli,[64] B. Franek,[64] E. O. Olaiya,[64] W. Roethel,[64] F. F. Wilson,[64] S. Emery,[65] M. Escalier,[65] A. Gaidot,[65] S. F. Ganzhur,[65] G. Hamel de Monchenault,[65] W. Kozanecki,[65] G. Vasseur,[65] Ch. Yèche,[65] M. Zito,[65] X. R. Chen,[66] H. Liu,[66] W. Park,[66] M. V. Purohit,[66] R. M. White,[66] J. R. Wilson,[66] M. T. Allen,[67] D. Aston,[67] R. Bartoldus,[67] P. Bechtle,[67] R. Claus,[67] J. P. Coleman,[67] M. R. Convery,[67] J. C. Dingfelder,[67] J. Dorfan,[67] G. P. Dubois-Felsmann,[67] W. Dunwoodie,[67] R. C. Field,[67] T. Glanzman,[67] S. J. Gowdy,[67] M. T. Graham,[67] P. Grenier,[67] C. Hast,[67] W. R. Innes,[67] J. Kaminski,[67] M. H. Kelsey,[67] H. Kim,[67] P. Kim,[67] M. L. Kocian,[67] D. W. G. S. Leith,[67] S. Li,[67] S. Luitz,[67] V. Luth,[67] H. L. Lynch,[67] D. B. MacFarlane,[67] H. Marsiske,[67] R. Messner,[67] D. R. Muller,[67] S. Nelson,[67] C. P. O'Grady,[67] I. Ofte,[67] A. Perazzo,[67] M. Perl,[67] T. Pulliam,[67] B. N. Ratcliff,[67] A. Roodman,[67] A. A. Salnikov,[67] R. H. Schindler,[67] J. Schwiening,[67] A. Snyder,[67] D. Su,[67] M. K. Sullivan,[67] K. Suzuki,[67] S. K. Swain,[67] J. M. Thompson,[67] J. Va'vra,[67] A. P. Wagner,[67] M. Weaver,[67] W. J. Wisniewski,[67] M. Wittgen,[67] D. H. Wright,[67] A. K. Yarritu,[67] K. Yi,[67] C. C. Young,[67] V. Ziegler,[67] P. R. Burchat,[68] A. J. Edwards,[68] S. A. Majewski,[68] T. S. Miyashita,[68] B. A. Petersen,[68] L. Wilden,[68] S. Ahmed,[69] M. S. Alam,[69] R. Bula,[69] J. A. Ernst,[69] B. Pan,[69] M. A. Saeed,[69] F. R. Wappler,[69] S. B. Zain,[69] S. M. Spanier,[70] B. J. Wogsland,[70] R. Eckmann,[71] J. L. Ritchie,[71] A. M. Ruland,[71] C. J. Schilling,[71] R. F. Schwitters,[71] J. M. Izen,[72] X. C. Lou,[72] S. Ye,[72] F. Bianchi,[73] F. Gallo,[73] D. Gamba,[73] M. Pelliccioni,[73] M. Bomben,[74] L. Bosisio,[74] C. Cartaro,[74] F. Cossutti,[74] G. Della Ricca,[74] L. Lanceri,[74] L. Vitale,[74] V. Azzolini,[75] N. Lopez-March,[75] F. Martinez-Vidal,[75,¶] D. A. Milanes,[75] A. Oyanguren,[75] J. Albert,[76] Sw. Banerjee,[76] B. Bhuyan,[76] K. Hamano,[76] R. Kowalewski,[76] I. M. Nugent,[76] J. M. Roney,[76] R. J. Sobie,[76] P. F. Harrison,[77] J. Ilic,[77] T. E. Latham,[77] G. B. Mohanty,[77] H. R. Band,[78] X. Chen,[78] S. Dasu,[78] K. T. Flood,[78] J. J. Hollar,[78] P. E. Kutter,[78] Y. Pan,[78] M. Pierini,[78] R. Prepost,[78] S. L. Wu,[78] and H. Neal[79]

[1]*Laboratoire de Physique des Particules, IN$_2$P$_3$/CNRS et Université de Savoie, F-74941 Annecy-Le-Vieux, France*
[2]*Universitat de Barcelona, Facultat de Fisica, Departament ECM, E-08028 Barcelona, Spain*
[3]*Università di Bari, Dipartimento di Fisica and INFN, I-70126 Bari, Italy*
[4]*University of Bergen, Institute of Physics, N-5007 Bergen, Norway*
[5]*Lawrence Berkeley National Laboratory and University of California, Berkeley, California 94720, USA*
[6]*University of Birmingham, Birmingham, B15 2TT, United Kingdom*
[7]*Ruhr Universität Bochum, Institut für Experimentalphysik 1, D-44780 Bochum, Germany*
[8]*University of Bristol, Bristol BS8 1TL, United Kingdom*
[9]*University of British Columbia, Vancouver, British Columbia, Canada V6T 1Z1*
[10]*Brunel University, Uxbridge, Middlesex UB8 3PH, United Kingdom*
[11]*Budker Institute of Nuclear Physics, Novosibirsk 630090, Russia*
[12]*University of California at Irvine, Irvine, California 92697, USA*
[13]*University of California at Los Angeles, Los Angeles, California 90024, USA*
[14]*University of California at Riverside, Riverside, California 92521, USA*
[15]*University of California at San Diego, La Jolla, California 92093, USA*
[16]*University of California at Santa Barbara, Santa Barbara, California 93106, USA*
[17]*University of California at Santa Cruz, Institute for Particle Physics, Santa Cruz, California 95064, USA*
[18]*California Institute of Technology, Pasadena, California 91125, USA*
[19]*University of Cincinnati, Cincinnati, Ohio 45221, USA*
[20]*University of Colorado, Boulder, Colorado 80309, USA*
[21]*Colorado State University, Fort Collins, Colorado 80523, USA*
[22]*Universität Dortmund, Institut für Physik, D-44221 Dortmund, Germany*
[23]*Technische Universität Dresden, Institut für Kern- und Teilchenphysik, D-01062 Dresden, Germany*
[24]*Laboratoire Leprince-Ringuet, CNRS/IN$_2$P$_3$, Ecole Polytechnique, F-91128 Palaiseau, France*
[25]*University of Edinburgh, Edinburgh EH9 3JZ, United Kingdom*
[26]*Università di Ferrara, Dipartimento di Fisica and INFN, I-44100 Ferrara, Italy*
[27]*Laboratori Nazionali di Frascati dell'INFN, I-00044 Frascati, Italy*
[28]*Università di Genova, Dipartimento di Fisica and INFN, I-16146 Genova, Italy*
[29]*Harvard University, Cambridge, Massachusetts 02138, USA*
[30]*Universität Heidelberg, Physikalisches Institut, Philosophenweg 12, D-69120 Heidelberg, Germany*
[31]*Imperial College London, London, SW7 2AZ, United Kingdom*
[32]*University of Iowa, Iowa City, Iowa 52242, USA*
[33]*Iowa State University, Ames, Iowa 50011-3160, USA*

[34]Johns Hopkins University, Baltimore, Maryland 21218, USA
[35]Universität Karlsruhe, Institut für Experimentelle Kernphysik, D-76021 Karlsruhe, Germany
[36]Laboratoire de l'Accélérateur Linéaire, IN_2P_3/CNRS et Université Paris-Sud 11, Centre Scientifique d'Orsay, B. P. 34, F-91898 ORSAY Cedex, France
[37]Lawrence Livermore National Laboratory, Livermore, California 94550, USA
[38]University of Liverpool, Liverpool L69 7ZE, United Kingdom
[39]Queen Mary, University of London, E1 4NS, United Kingdom
[40]University of London, Royal Holloway and Bedford New College, Egham, Surrey TW20 0EX, United Kingdom
[41]University of Louisville, Louisville, Kentucky 40292, USA
[42]University of Manchester, Manchester M13 9PL, United Kingdom
[43]University of Maryland, College Park, Maryland 20742, USA
[44]University of Massachusetts, Amherst, Massachusetts 01003, USA
[45]Massachusetts Institute of Technology, Laboratory for Nuclear Science, Cambridge, Massachusetts 02139, USA
[46]McGill University, Montréal, Québec, Canada H3A 2T8
[47]Università di Milano, Dipartimento di Fisica and INFN, I-20133 Milano, Italy
[48]University of Mississippi, University, Mississippi 38677, USA
[49]Université de Montréal, Physique des Particules, Montréal, Québec, Canada H3C 3J7
[50]Mount Holyoke College, South Hadley, Massachusetts 01075, USA
[51]Università di Napoli Federico II, Dipartimento di Scienze Fisiche and INFN, I-80126, Napoli, Italy
[52]NIKHEF, National Institute for Nuclear Physics and High Energy Physics, NL-1009 DB Amsterdam, The Netherlands
[53]University of Notre Dame, Notre Dame, Indiana 46556, USA
[54]Ohio State University, Columbus, Ohio 43210, USA
[55]University of Oregon, Eugene, Oregon 97403, USA
[56]Università di Padova, Dipartimento di Fisica and INFN, I-35131 Padova, Italy
[57]Laboratoire de Physique Nucléaire et de Hautes Energies, IN_2P_3/CNRS, Université Pierre et Marie Curie-Paris6, Université Denis Diderot-Paris7, F-75252 Paris, France
[58]University of Pennsylvania, Philadelphia, Pennsylvania 19104, USA
[59]Università di Perugia, Dipartimento di Fisica and INFN, I-06100 Perugia, Italy
[60]Università di Pisa, Dipartimento di Fisica, Scuola Normale Superiore and INFN, I-56127 Pisa, Italy
[61]Princeton University, Princeton, New Jersey 08544, USA
[62]Università di Roma La Sapienza, Dipartimento di Fisica and INFN, I-00185 Roma, Italy
[63]Universität Rostock, D-18051 Rostock, Germany
[64]Rutherford Appleton Laboratory, Chilton, Didcot, Oxon, OX11 0QX, United Kingdom
[65]DSM/Dapnia, CEA/Saclay, F-91191 Gif-sur-Yvette, France
[66]University of South Carolina, Columbia, South Carolina 29208, USA
[67]Stanford Linear Accelerator Center, Stanford, California 94309, USA
[68]Stanford University, Stanford, California 94305-4060, USA
[69]State University of New York, Albany, New York 12222, USA
[70]University of Tennessee, Knoxville, Tennessee 37996, USA
[71]University of Texas at Austin, Austin, Texas 78712, USA
[72]University of Texas at Dallas, Richardson, Texas 75083, USA
[73]Università di Torino, Dipartimento di Fisica Sperimentale and INFN, I-10125 Torino, Italy
[74]Università di Trieste, Dipartimento di Fisica and INFN, I-34127 Trieste, Italy
[75]IFIC, Universitat de Valencia-CSIC, E-46071 Valencia, Spain
[76]University of Victoria, Victoria, British Columbia, Canada V8W 3P6
[77]Department of Physics, University of Warwick, Coventry CV4 7AL, United Kingdom
[78]University of Wisconsin, Madison, Wisconsin 53706, USA
[79]Yale University, New Haven, Connecticut 06511, USA

(Received 28 October 2007; revised manuscript received 2 February 2008; published 23 May 2008)

This paper reports measurements of processes: $e^+e^- \to \gamma K^0_S K^\pm \pi^\mp$, $e^+e^- \to \gamma K^+K^-\pi^0$, $e^+e^- \to \gamma\phi\eta$, and $e^+e^- \to \gamma\phi\pi^0$. The initial-state radiated photon allows to cover the hadronic final state in the energy range from thresholds up to ≈ 4.6 GeV. The overall size of the data sample analyzed is 232 fb^{-1}, collected by the *BABAR* detector running at the PEP-II e^+e^- storage ring. From the Dalitz plot analysis of

[*]Deceased.
[+]Now at Tel Aviv University, Tel Aviv, 69978, Israel.
[‡]Also with Università di Perugia, Dipartimento di Fisica, Perugia, Italy.
[§]Also with Università della Basilicata, Potenza, Italy.
[‖]Also with Universita' di Sassari, Sassari, Italy.
[¶]Also with Universitat de Barcelona, Facultat de Fisica, Departament ECM, E-08028 Barcelona, Spain.

the $K^0_S K^\pm \pi^\mp$ final state, moduli, and relative phase of the isoscalar and the isovector components of the $e^+e^- \to KK^*(892)$ cross section are determined. Parameters of ϕ and ρ recurrences are also measured, using a global fitting procedure which exploits the interconnection among amplitudes, moduli, and phases of the $e^+e^- \to K^0_S K^\pm \pi^\mp$, $K^+K^-\pi^0$, $\phi\eta$ final states. The cross section for the OZI-forbidden process $e^+e^- \to \phi\pi^0$, and the J/ψ branching fractions to $KK^*(892)$ and $K^+K^-\eta$ are also measured.

DOI: 10.1103/PhysRevD.77.092002 PACS numbers: 13.66.Bc, 13.25.Gv, 13.25.Jx, 14.40.Cs

I. INTRODUCTION

The *BABAR* detector [1], designed to study time-dependent *CP*-violation in *B* decays, is very well suited to study hadronic final-state production. At an e^+e^- collider, lower center-of-mass (c.m.) energies can be studied using initial-state radiation (ISR). The possibility of exploiting such processes was first outlined in Ref. [2] and discussed in Refs. [3–5].

The cross section $\sigma_{\gamma f}$ to radiate a photon of energy E_γ and subsequently produce a definite hadronic final state f is related to the corresponding e^+e^- production cross section σ_f by

$$\frac{d\sigma_{\gamma f}(s,x)}{dx} = W(s,x)\cdot\sigma_f[s(1-x)], \qquad (1)$$

where $x = 2E_\gamma/\sqrt{s}$, $\sqrt{s}$ is the nominal e^+e^- c.m. energy, and $E_{\rm c.m.} \equiv \sqrt{s(1-x)}$ is the effective c.m. energy at which the final state f is produced. This quantity can be determined, for instance, by measuring the invariant mass of the hadronic final state. The radiator function $W(s,x)$, which describes the probability density for photon emission, can be evaluated with better than 1% accuracy (see, for example, Ref. [6]). The radiator function falls rapidly with increasing E_γ, but has a long tail, which produces sizeable event rates at very low $E_{\rm c.m.}$. In the present study we require the ISR photon to be detected in the *BABAR* electromagnetic calorimeter. The angular distribution of the ISR photon peaks along the beam direction, but 10%–15% [5] of the photons are emitted within the detector acceptance.

II. THE *BABAR* DETECTOR AND DATA SET

The data used in this analysis, collected with the *BABAR* detector at the PEP-II storage ring, correspond to an integrated luminosity of 232 fb^{-1}. Charged-particle momenta are measured in a tracking system consisting of a five-layer double-sided silicon vertex tracker (SVT) and a 40-layer central drift chamber (DCH), immersed in a 1.5 T axial magnetic field. An internally reflecting ring-imaging Cherenkov detector (DIRC) with quartz bar radiators provides charged-particle identification. A CsI electromagnetic calorimeter (EMC) is used to detect and identify photons and electrons. Muons are identified in the instrumented magnetic flux return system (IFR).

Electron candidates are selected using the ratio of the shower energy deposited in the EMC to the measured momentum, the shower shape, the specific ionization in the DCH, and the Cherenkov angle measured by the DIRC. Muons are identified by the depth of penetration into the IFR, the IFR cluster geometry, and the energy deposited in the EMC. Charged pion and kaon candidates are selected using a likelihood function based on the specific ionization in the DCH and SVT, and the Cherenkov angle measured in the DIRC. Photon candidates are defined as clusters in the EMC that have a shape consistent with an electromagnetic shower, without an associated charged track.

In order to study the detector acceptance and efficiency, a special package of simulation programs for radiative processes has been developed. Algorithms for generating hadronic final states via ISR are derived from Ref. [7]. Multiple soft-photon emission from initial-state charged particles is implemented by means of the structure-function technique [8,9], while extra photon radiation from final-state particles is simulated via the PHOTOS package [10].

The $e^+e^- \to K^0_S K^\pm \pi^\mp \gamma$, $K^+K^-\pi^0\gamma$, $\phi\eta\gamma$, and $\phi\pi^0\gamma$ reactions are simulated with the hadronic final states generated according to their phase space distributions. Both processes $e^+e^- \to P_1P_2P_3$ and $e^+e^- \to VP$ [7], where $P_{(i)}$ and V are pseudoscalar and vector mesons, respectively, are used in the simulation. To evaluate the backgrounds, a number of different ISR-produced final states, such as 4π, $KK\pi\pi$, and $\phi\pi^0\pi^0$, are simulated as well.

The quark-antiquark continuum production and hadronization ($q\bar{q}$ background in the following, where $q = u, d, s, c$) and $\tau\tau$ events are simulated using JETSET [11] and KORALB [12], respectively.

The generated events undergo a detector simulation based on GEANT4 [13] and are analyzed as experimental data.

III. EVENT SELECTION AND KINEMATICS

A preliminary set of selection criteria are applied to the data regardless of the final state under study. We consider only charged tracks emitted at a polar angle between 0.45 and 2.40 radians and that extrapolate within 0.25 cm of the beam axis and within 3 cm of the nominal collision point along the axis. We retain photon candidates with energy above 30 MeV and emitted at a polar angle between 0.35 and 2.40 radians. The highest-energy photon, assumed to be the ISR photon, is required to have an energy greater than 3 GeV.

We then apply channel specific selection criteria and subject each candidate event to a one-constraint (1C) kine-

matic fit, both to select the signal and to estimate the background contamination. The fit uses as input the measured quantities (momenta and angles) of the selected charged tracks and photons, together with the associated error matrices. However, because of the excellent resolution of the DCH, the three-momentum vector of the ISR photon is better determined through the momentum conservation than through the measurement in the EMC, thus reducing the number of constraints to one. For final states containing a π^0 or an η, we perform the kinematic fit for every possible pair of detected photons, without applying a mass constraint, and retain the pair producing the lowest χ^2. The fitting procedure predicts the ISR photon direction, which is then required to be consistent with the observed ISR photon within 15 mrad. In order to reduce multiphoton events, we also require that no more than 400 MeV of additional neutral energy, besides the ISR and π^0 (η) decay photons, be detected in the EMC. This cut has no effect on signal events.

We select as π^0 (η) candidates $\gamma\gamma$ pairs whose masses lie in the range 0.110–0.160 (0.520–0.580) GeV/c^2. In calculating the invariant masses of these pairs, we use the photon momenta resulting from the 1 C fits described above. This improves the π^0, η mass resolution by $\approx$ 20%. To get rid of the contamination due to additional soft photons produced by machine background or by interactions in the detector material, we require both photons used for π^0 or η candidates to have an energy greater than 60 MeV and at least one cluster containing more than 100 MeV.

As K^0_S candidates, we select pairs of charged tracks forming a vertex with a good χ^2 at least 2 mm away from the event primary vertex, and whose $\pi^+\pi^-$ invariant mass lies within 15 MeV/c^2 of the nominal K^0_S mass. We also require that $\theta_{K^0_S}$, the angle between the K^0_S momentum vector and the line connecting the K^0_S vertex to the primary vertex position, satisfy the condition $\cos(\theta_{K^0_S}) > 0.99$. For the purposes of the 1C fit described earlier, the K^0_S candidate is treated as a single particle and its covariance matrix is used as the corresponding track covariance matrix.

Charged kaon and pion candidates are selected using likelihood ratios for the hypotheses e, μ, π, K, and p based upon specific ionization measurements in the SVT and DCH, and Cherenkov light observed in the DIRC. The algorithm used here for $K^\pm$ identification is over 80% efficient in the momentum range of interest, with π, μ, p, $e \to K$ misidentification rates well below 2%.

IV. THE $K^0_S K^\pm \pi^\mp$ FINAL STATE

A. Event selection

We require exactly four charged tracks with zero net charge, two of them coming from the primary vertex of the event and identified, respectively, as a kaon and a pion, and the other two forming a K^0_S.

Figure 1 shows the χ^2 distribution of the selected data sample, together with three different Monte Carlo (MC) simulations: signal events, background contribution due to $e^+e^- \to q\bar{q}$, and ISR-produced processes $K^+K^-\pi^+\pi^- + 2(\pi^+\pi^-)$ that might mimic this final state. A total of 3860 events are selected within the χ^2 signal region, i.e., $\chi^2 < 20$.

The background due to misreconstructed K^0_S is small, as can be inferred from the K^0_S mass distribution shown in Fig. 2, and it is almost exclusively given by the reactions $e^+e^- \to \gamma K^+K^-\pi^+\pi^-$ and $e^+e^- \to \gamma\pi^+\pi^-\pi^+\pi^-$. These processes differ from the signal only by one $K-\pi$ exchange, and produce a χ^2 distribution peaking at low values. The direct simulation of these two sources of background yields to respectively 44 ± 15 and 10 ± 5 events in the χ^2 signal region, where the errors are taken from the uncertainties of the corresponding production cross sections [14].

The cross sections for the background processes in continuum $q\bar{q}$ production are poorly known; this type of background is almost exclusively produced by processes like $e^+e^- \to K^0_S K^\pm \pi^\mp \pi^0$ with the π^0 decaying into two very energetically asymmetric photons and/or photons merged in a single EMC cluster that fake the ISR photon. This class of events, as a consequence, produces a sharp peak at the π^0 invariant mass when the fake ISR photon is combined with another photon in the event.

Figure 3(a) depicts the invariant mass combination of the candidate ISR photon with any other photon in the event. A sharp peak at the π^0 mass is evident for the $q\bar{q}$ MC

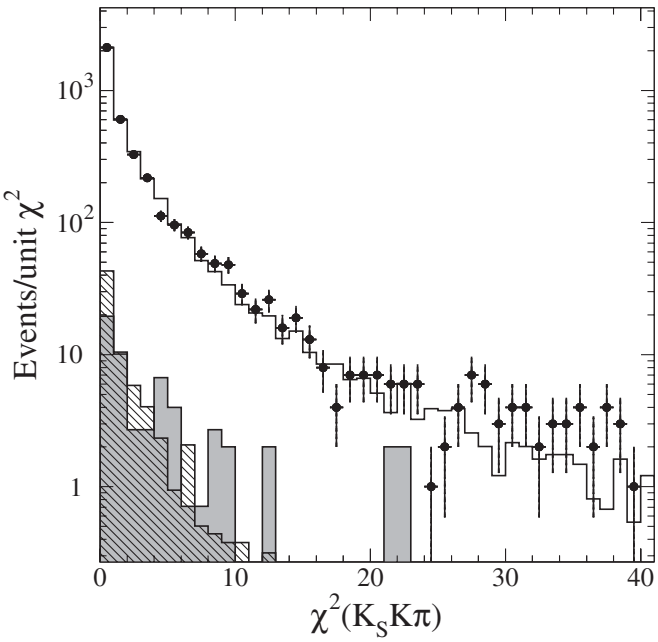

FIG. 1. The χ^2 distributions for data (points), signal MC (open histogram) normalized to the first bin of the data, background contribution due to $q\bar{q}$ (hatched histogram), and different ISR-produced final states (gray histogram).

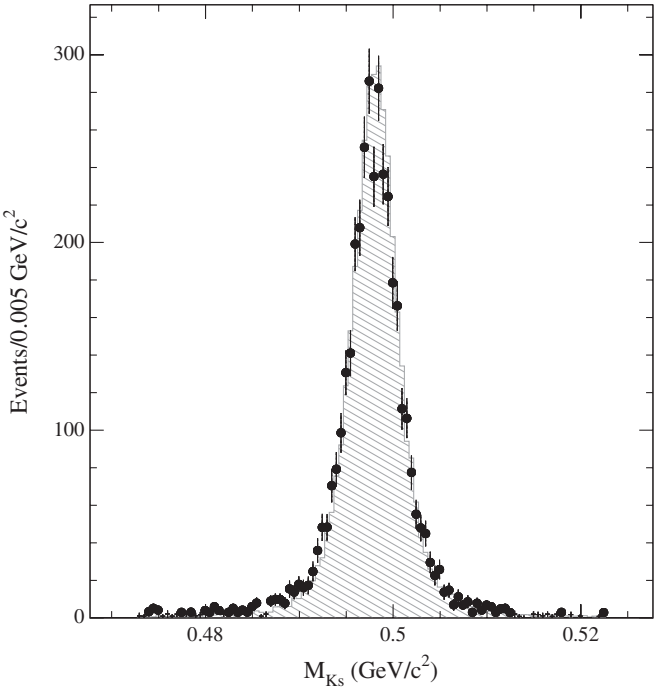

FIG. 2. Reconstructed K^0_S mass for data (points) and signal MC simulation (histogram).

sample, while the signal and the data distributions are both essentially flat in that region. We perform a fit to the data distribution, combining with weights the distributions of $q\bar{q}$ background and signal. The difference between the shapes of the signal and $q\bar{q}$ distributions allows to obtain unambiguously the weights from the fit. We find a weight for the $q\bar{q}$ of about $1/9$, which translates into 72 ± 42 $q\bar{q}$ background events.

Any remaining background due to other ISR processes should result in a relatively flat χ^2 distribution, as a consequence of the misreconstructed final state. We check the consistency of the χ^2 distribution by normalizing the data and the simulated $K^0_S K^{\pm}\pi^{\mp}$ sample to the first bin of the data distribution (see Fig. 1), after subtracting the already estimated background components. The difference between data and normalized signal distributions gives an estimate of additional background events consistent with zero.

As a cross-check, we show in Fig. 3(b) the invariant mass distribution of any pair of detected photons in the event, not including the ISR photon. The very good agreement between the data and the simulated signal sample and the absence of a peak at the π^0 mass, confirm that background contribution from final states with extra π^0's is negligible.

The $K^0_S K^{\pm}\pi^{\mp}$ invariant mass distribution for the final sample is shown in Fig. 4, together with the estimated $q\bar{q}$ and ISR backgrounds. The final signal yield after background subtraction consists of 3734 events.

B. Cross section for $e^+e^- \to K^0_S K^{\pm}\pi^{\mp}$

The cross section for the $e^+e^- \to K^0_S K^{\pm}\pi^{\mp}$ process as a function of the effective c.m. energy, $E_{\rm c.m.}$, is evaluated from

$$\sigma_{e^+e^-\to K^0_S K^{\pm}\pi^{\mp}}(E_{\rm c.m.}) = \frac{dN_{K^0_S K\pi\gamma}(E_{\rm c.m.})}{d\mathcal{L}(E_{\rm c.m.})\cdot\epsilon(E_{\rm c.m.})}, \qquad (2)$$

where $E_{\rm c.m.}$ is the invariant mass of the reconstructed $K^0_S K^{\pm}\pi^{\mp}$ system, $dN_{K^0_S K\pi\gamma}$ is the number of selected $K^0_S K^{\pm}\pi^{\mp}$ events after background subtraction in the interval $dE_{\rm c.m.}$, and $\epsilon(E_{\rm c.m.})$ is the corresponding detection efficiency obtained from the signal MC simulation. The differential luminosity, $d\mathcal{L}(E_{\rm c.m.})$, in each interval $dE_{\rm c.m.}$, is evaluated from ISR $\mu\mu\gamma$ events with the photon in the same fiducial range used for simulation; the procedure is described in Refs. [15,16]. From data-simulation compari-

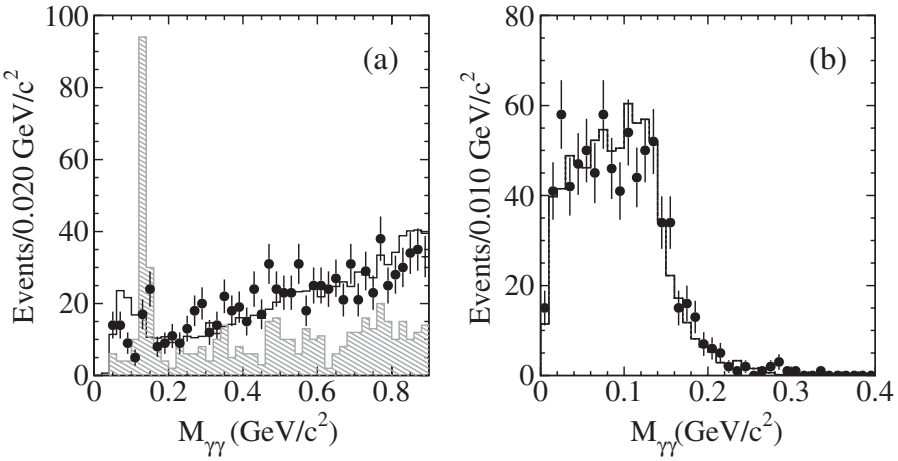

FIG. 3. (a) Invariant mass of the ISR photon and any other photon in the event. Distributions for data (points with error bars), signal MC (open histogram), and $q\bar{q}$ MC (hatched histogram) samples are shown. (b) $\gamma\gamma$ mass distribution for additional photons in data (points) compared with signal MC simulation.

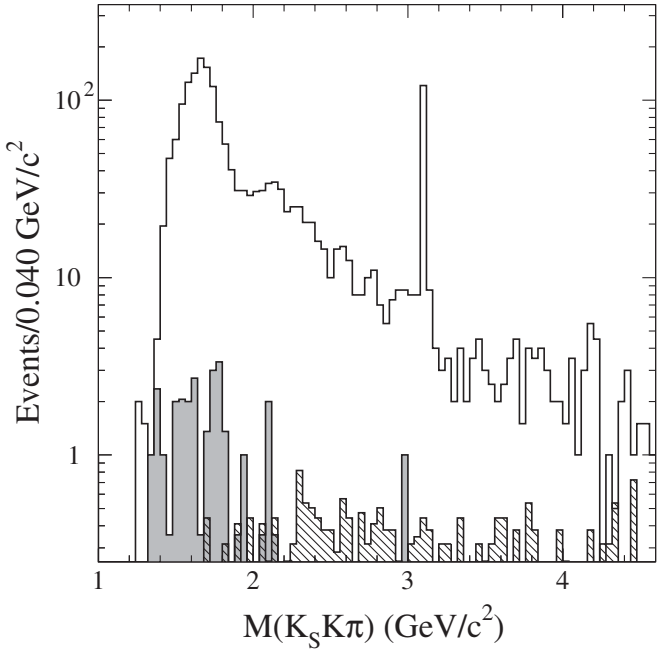

FIG. 4. The invariant mass distribution of the $K^0_S K^\pm \pi^\mp$ system (open histogram). The hatched and gray histograms show the $q\bar{q}$ and ISR backgrounds, respectively.

son, we conservatively estimate a systematic uncertainty of 3.0% on $d\mathcal{L}$. This error also includes the uncertainties on radiative corrections, estimated from a MC simulation to be $\approx 1\%$.

The efficiency, which accounts also for the $K^0_S \to \pi^+\pi^-$ decay rate, has been corrected for differences between data and simulation: the angular distributions are different from the simulated distributions because the latter, based on a phase space model, do not account for the presence of intermediate resonant states. However, the angular acceptance is essentially uniform for ISR events, so the uncertainty in estimated efficiencies due to imprecise modeling of the process dynamics is, at most, 3.0%. We study several control samples to determine any difference on track reconstruction efficiency between data and simulation. We find that the MC efficiency is overestimated by 0.8% per charged track, with an uncertainty of $\pm 0.5\%$. Analogously, we determine a correction of 2.6% on the K^0_S reconstruction efficiency, with an associated systematic uncertainty of 1.1%. The uncertainties on $q\bar{q}$ and ISR-background estimates lead to systematic errors of 1.1% and 0.5%, respectively.

The main systematic uncertainties assigned to the measurement are summarized in Table I. The corrections applied to the measured cross sections sum to $+4.2\%$, while the estimated total systematic error is $\pm 5.1\%$.

For a typical ISR reaction, the selection efficiency is expected to have a smooth behavior as a function of $E_{\text{c.m.}}$. Therefore, we fit the efficiency values obtained from MC as shown in Fig. 5, and use the fit result, together with the estimated corrections, to obtain the cross section plotted in

TABLE I. Summary of corrections and systematic errors applied to the $e^+e^- \to K^0_S K^\pm \pi^\mp$ cross section measurement.

Source	Correction	Systematic error
ISR luminosity	—	3.0%
$q\bar{q}$ background	—	1.1%
ISR background	—	0.5%
Track reconstruction efficiency	+1.6%	1.0%
PID efficiency	—	2.0%
K^0_S reconstruction efficiency	+2.6%	1.1%
$\mathcal{B}(K^0_S \to \pi^+\pi^-)$ [17]	—	0.7%
MC model	—	3.0%
Total	+4.2%	5.1%

Fig. 6. The cross section has a maximum of about 3.8 nb around 1.65 GeV, and a long tail. The only clear structure observed at higher energies is the J/ψ. In the inset of the same figure the cross section at energies higher than the J/ψ is shown: there is no evidence of the recently discovered $Y(4260)$ resonance [18], we obtain an upper limit for $\Gamma^{Y(4260)}_{ee}\mathcal{B}^{Y(4260)}_{K^0_S K^\pm \pi^\mp}$ of 0.5 eV at 90% confidence level (C.L.), where $\Gamma^{Y(4260)}_{ee}$ is the $Y(4260) \to e^+e^-$ width and $\mathcal{B}^{Y(4260)}_{K^0_S K^\pm \pi^\mp}$ is the branching fraction for $Y(4260) \to K^0_S K^\pm \pi^\mp$. An excess of events is observed at ≈ 4.2 GeV: there are 15 events in a 40 MeV energy window, to be compared to an expectation of 5 events, corresponding to a probability of 2.2×10^{-4} to be a statistical fluctuation of the cross section.

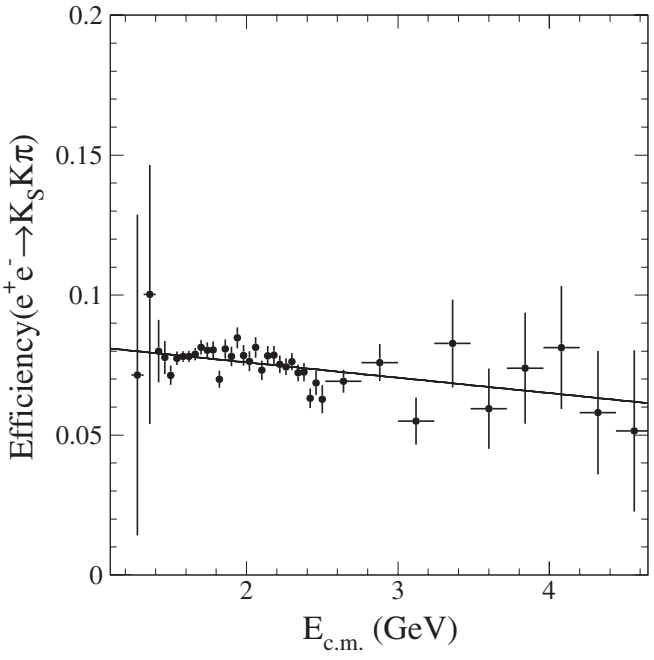

FIG. 5. Detection and reconstruction efficiency as a function of the c.m. energy for the $K^0_S K^\pm \pi^\mp$ final state. The solid line is the result of a linear fit to the data.

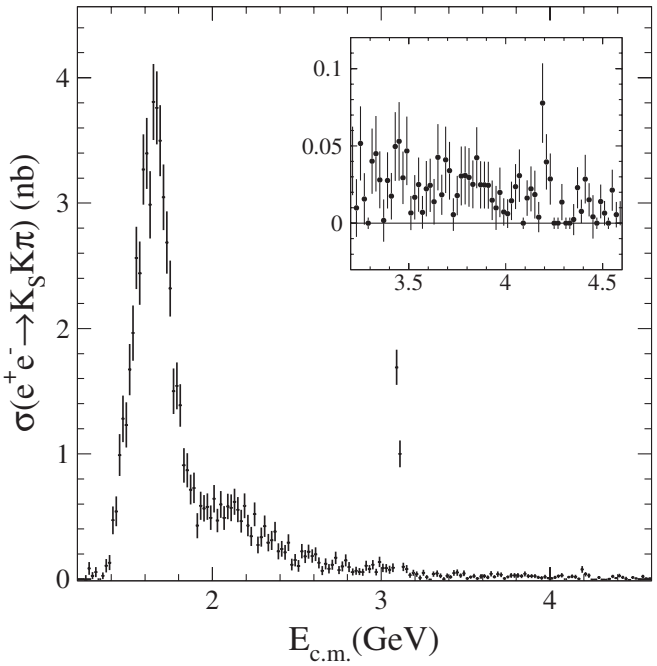

FIG. 6. The $e^+e^- \to K^0_S K^\pm \pi^\mp$ cross section. Inset: expanded view in the mass range $3.2 < E_{\rm c.m.} < 4.6$ GeV.

The values of the measured cross section are reported in Table II with the corresponding statistical errors. Figure 7 shows a compilation of the measured cross section as obtained by previous direct e^+e^- experiments (data are available only up to 2.4 GeV [19]). The data show reasonable consistency; our measurements, however, have much smaller statistical and systematic errors.

V. THE $K^+K^-\pi^0$ FINAL STATE

We select $K^+K^-\pi^0$ candidate events by requiring two charged tracks identified as kaons, and two photons forming a π^0 candidate, in addition to the ISR photon. In order to avoid any possible contamination from events with intermediate $\phi \to K^+K^-$ production, we require $M_{KK} > 1.045$ GeV$/c^2$, where M_{KK} is the invariant mass of the K^+K^- system. As previously described, we perform the kinematic fit for every possible pair of selected photons and we retain for each event the $\gamma\gamma$ combination giving the lowest χ^2. Figure 8 shows the χ^2 distribution of the selected data sample and the normalized distributions of signal MC simulation and different background sources

TABLE II. Measurement of the $e^+e^- \to K^0_S K^\pm \pi^\mp$ cross section as a function of $E_{\rm c.m.}$. Errors are statistical only.

$E_{\rm c.m.}$ (GeV)	σ (nb)	$E_{\rm c.m.}$ (GeV)	σ (nb)	$E_{\rm c.m.}$ (GeV)	σ (nb)	$E_{\rm c.m.}$ (GeV)	σ (nb)
1.24–1.28	0.037 ± 0.034	1.96–1.98	0.578 ± 0.105	2.62–2.64	0.131 ± 0.044	3.30–3.34	0.043 ± 0.016
1.28–1.32	0.042 ± 0.024	1.98–2.00	0.491 ± 0.098	2.64–2.66	0.068 ± 0.036	3.34–3.38	0.015 ± 0.011
1.32–1.36	0.014 ± 0.014	2.00–2.02	0.642 ± 0.109	2.66–2.68	0.122 ± 0.044	3.38–3.42	0.023 ± 0.012
1.36–1.38	0.107 ± 0.054	2.02–2.04	0.469 ± 0.093	2.68–2.70	0.083 ± 0.037	3.42–3.46	0.051 ± 0.017
1.38–1.40	0.132 ± 0.059	2.04–2.06	0.597 ± 0.107	2.70–2.72	0.116 ± 0.040	3.46–3.50	0.038 ± 0.014
1.40–1.42	0.470 ± 0.111	2.06–2.08	0.488 ± 0.095	2.72–2.74	0.170 ± 0.050	3.50–3.54	0.012 ± 0.009
1.42–1.44	0.542 ± 0.118	2.08–2.10	0.581 ± 0.102	2.74–2.76	0.073 ± 0.033	3.54–3.58	0.016 ± 0.010
1.44–1.46	0.990 ± 0.167	2.10–2.12	0.569 ± 0.107	2.76–2.78	0.102 ± 0.041	3.58–3.62	0.023 ± 0.012
1.46–1.48	1.279 ± 0.187	2.12–2.14	0.619 ± 0.104	2.78–2.80	0.151 ± 0.048	3.62–3.66	0.028 ± 0.013
1.48–1.50	1.231 ± 0.180	2.14–2.16	0.555 ± 0.099	2.80–2.82	0.097 ± 0.041	3.66–3.70	0.030 ± 0.013
1.50–1.52	1.673 ± 0.205	2.16–2.18	0.463 ± 0.091	2.82–2.84	0.058 ± 0.029	3.70–3.74	0.020 ± 0.011
1.52–1.54	1.964 ± 0.220	2.18–2.20	0.586 ± 0.100	2.84–2.86	0.067 ± 0.032	3.74–3.78	0.024 ± 0.011
1.54–1.56	2.564 ± 0.249	2.20–2.22	0.428 ± 0.085	2.86–2.88	0.060 ± 0.028	3.78–3.82	0.030 ± 0.013
1.56–1.58	2.440 ± 0.253	2.22–2.24	0.342 ± 0.076	2.88–2.90	0.056 ± 0.028	3.82–3.86	0.034 ± 0.013
1.58–1.60	3.269 ± 0.282	2.24–2.26	0.518 ± 0.095	2.90–2.92	0.108 ± 0.040	3.86–3.90	0.025 ± 0.011
1.60–1.62	3.397 ± 0.283	2.26–2.28	0.272 ± 0.067	2.92–2.94	0.081 ± 0.032	3.90–3.94	0.020 ± 0.010
1.62–1.64	2.987 ± 0.268	2.28–2.30	0.336 ± 0.077	2.94–2.96	0.116 ± 0.038	3.94–3.98	0.015 ± 0.011
1.64–1.66	3.807 ± 0.302	2.30–2.32	0.422 ± 0.086	2.96–2.98	0.058 ± 0.027	3.98–4.02	0.007 ± 0.006
1.66–1.68	3.760 ± 0.291	2.32–2.34	0.291 ± 0.069	2.98–3.00	0.138 ± 0.041	4.02–4.06	0.019 ± 0.010
1.68–1.70	3.498 ± 0.284	2.34–2.36	0.310 ± 0.076	3.00–3.02	0.090 ± 0.033	4.06–4.10	0.015 ± 0.008
1.70–1.72	3.046 ± 0.262	2.36–2.38	0.381 ± 0.077	3.02–3.04	0.088 ± 0.033	4.10–4.14	0.019 ± 0.009
1.72–1.74	2.686 ± 0.247	2.38–2.40	0.222 ± 0.064	3.04–3.06	0.075 ± 0.031	4.14–4.18	0.011 ± 0.009
1.74–1.76	2.319 ± 0.223	2.40–2.42	0.242 ± 0.064	3.06–3.08	0.091 ± 0.036	4.18–4.22	0.059 ± 0.016
1.76–1.78	1.500 ± 0.181	2.42–2.44	0.215 ± 0.059	3.08–3.10	1.690 ± 0.140	4.22–4.26	0.013 ± 0.009
1.78–1.80	1.543 ± 0.187	2.44–2.46	0.291 ± 0.067	3.10–3.12	0.999 ± 0.106	4.26–4.30	0.006 ± 0.006
1.80–1.82	1.387 ± 0.170	2.46–2.48	0.116 ± 0.047	3.12–3.14	0.098 ± 0.033	4.30–4.38	0.005 ± 0.004
1.82–1.84	0.908 ± 0.136	2.48–2.50	0.153 ± 0.049	3.14–3.16	0.081 ± 0.032	4.38–4.46	0.014 ± 0.006
1.84–1.86	0.869 ± 0.137	2.50–2.52	0.106 ± 0.047	3.16–3.18	0.031 ± 0.019	4.46–4.54	0.003 ± 0.004
1.86–1.88	0.714 ± 0.119	2.52–2.54	0.223 ± 0.058	3.18–3.20	0.051 ± 0.025	4.54–4.62	0.011 ± 0.005
1.88–1.90	0.729 ± 0.122	2.54–2.56	0.181 ± 0.051	3.20–3.22	0.040 ± 0.022	4.62–4.70	0.003 ± 0.004
1.90–1.92	0.427 ± 0.099	2.56–2.58	0.219 ± 0.057	3.22–3.24	0.010 ± 0.019		
1.92–1.94	0.586 ± 0.111	2.58–2.60	0.184 ± 0.053	3.24–3.26	0.052 ± 0.024		
1.94–1.96	0.565 ± 0.105	2.60–2.62	0.200 ± 0.054	3.26–3.30	0.007 ± 0.009		

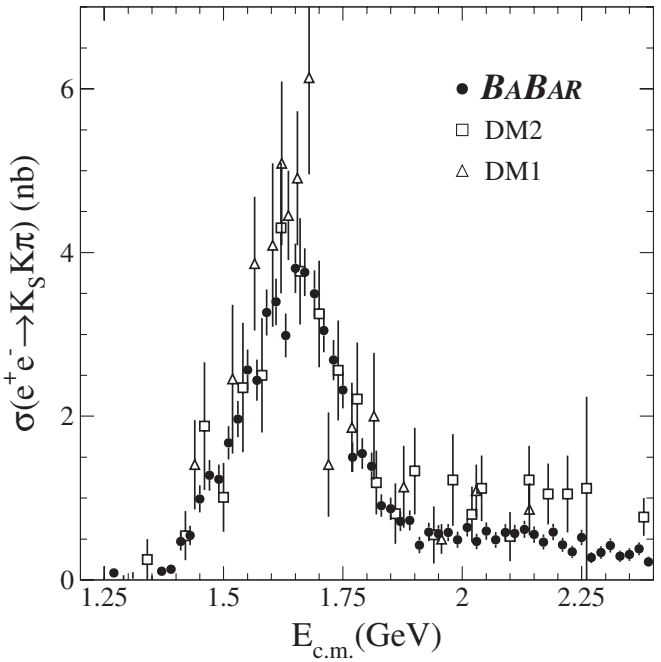

FIG. 7. Comparison of the $e^+e^- \to K^0_S K^\pm \pi^\mp$ cross section measured in *BABAR* with previous experiments, in the mass range $1.3 < E_{\rm c.m.} < 2.4$ GeV.

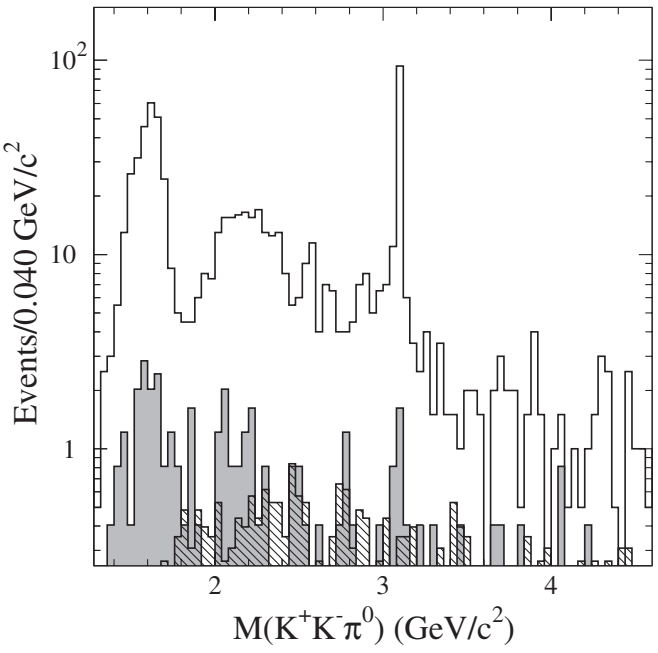

FIG. 9. The invariant mass distribution of the $K^+K^-\pi^0$ system (open histogram). The hatched and gray histograms show the $q\bar{q}$ and ISR backgrounds, respectively.

($q\bar{q}$ and $e^+e^- \to \omega\gamma \to \pi^+\pi^-\pi^0\gamma$). The selection procedure results in 1524 events with a $\chi^2 < 20$.

Applying a procedure analogous to the one described in the previous section for the $K^0_S K^\pm \pi^\mp$ analysis, we determine 62 ± 35 $q\bar{q}$ and 84 ± 27 ISR-background events from different ISR processes. The mass spectrum of the selected sample is shown in Fig. 9, together with the estimated $q\bar{q}$ and ISR backgrounds. After background subtraction, 1378 signal events are retained.

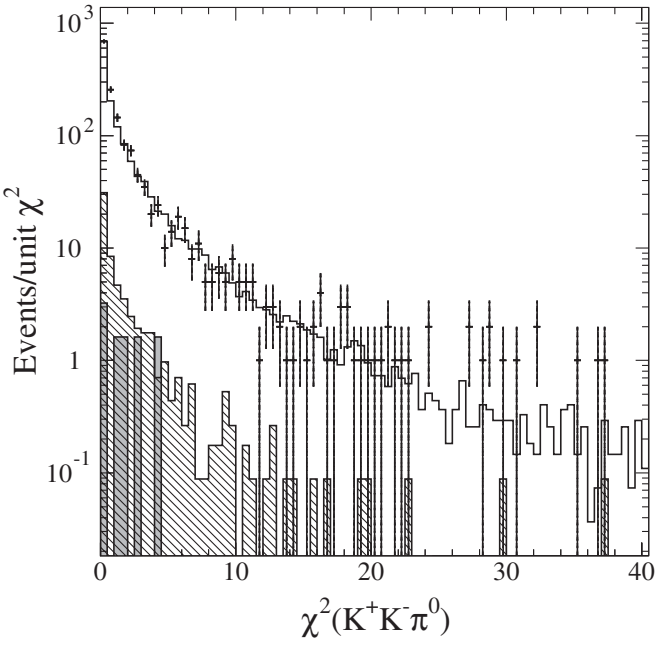

FIG. 8. The χ^2 distributions for data (points), signal MC simulation (open histogram) normalized to the first bin of the data, background contributions due to $q\bar{q}$ (hatched histogram), and to $e^+e^- \to \omega\gamma \to \pi^+\pi^-\pi^0\gamma$ MC simulation (gray histogram).

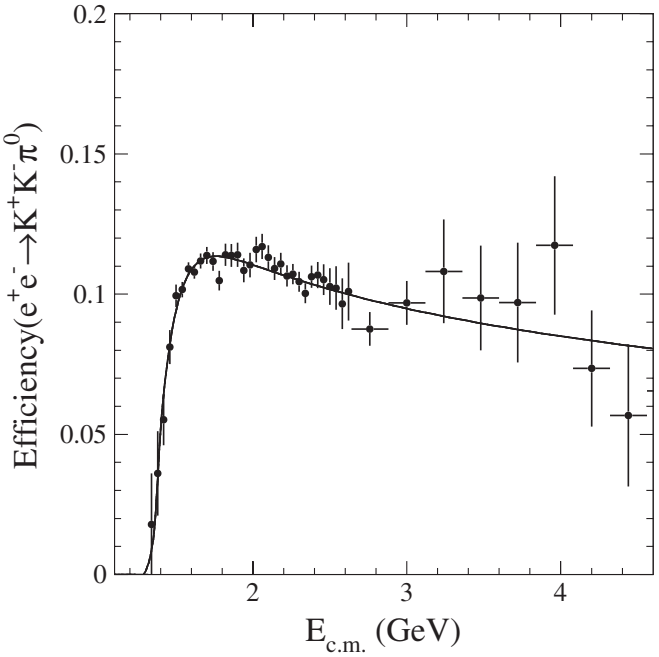

FIG. 10. Detection and reconstruction efficiency as a function of the c.m. energy for $K^+K^-\pi^0$ final state. The solid line is the result of a fit to the data with the function $a(1-(x/b)^p \cdot e^{\xi(b-x)})$, where $x = E_{\rm c.m.}$.

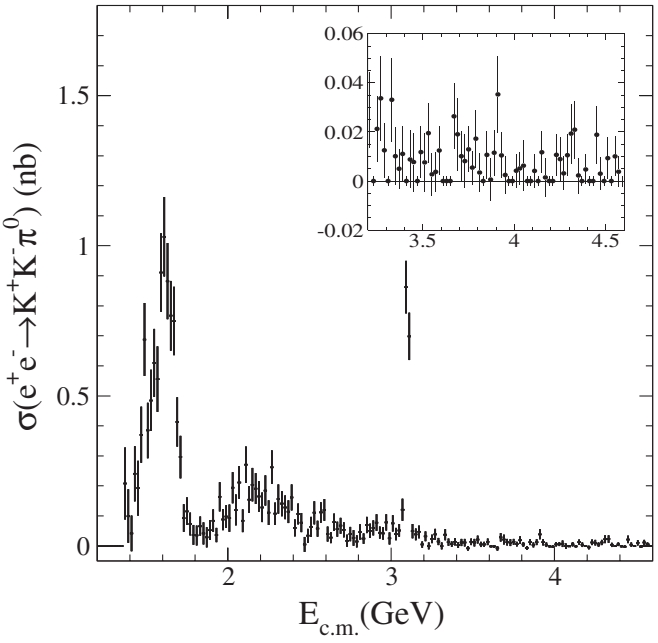

FIG. 11. The $e^+e^- \to K^+K^-\pi^0$ cross section. Inset: expanded view in the $3.2 < E_{\rm c.m.} < 4.6$ GeV mass range.

As in the $K^0_S K^\pm \pi^\mp$ channel, we measure the $e^+e^- \to K^+K^-\pi^0$ cross section as a function of the effective c.m. energy, in 20 MeV energy bins. The reconstruction and selection efficiency for each energy interval is shown in Fig. 10, while the corresponding cross section values are shown in Fig. 11 and reported in Table III (variable width bin size). Figure 12 shows a comparison with the DM2 measurement [19].

The cross section values shown in Fig. 11 include only statistical errors. The inset of the same figure is an enlarged view of the 3.3–4.6 GeV energy region, there is no evidence of the $Y(4260)$, and we estimate an upper limit for $\Gamma^{Y(4260)}_{ee}\mathcal{B}^{Y(4260)}_{K^+K^-\pi^0}$ of 0.6 eV at 90% C.L. The systematic errors are summarized in Table IV, along with the corrections applied to the cross section measurements [15,16]. The correction and systematic error associated with the MC/data difference in the π^0 reconstruction efficiency have been studied using the ISR-produced high statistics channel $\omega\pi^0 \to \pi^+\pi^-\pi^0\pi^0$ [16]. It has been found that the MC efficiency is $3.0 \pm 3.0\%$ higher than the data. The corrections applied to the measured cross sections sum to

TABLE III. Measurement of the $e^+e^- \to K^+K^-\pi^0$ cross section as a function of $E_{\rm c.m.}$. Errors are statistical only.

$E_{\rm c.m.}$ (GeV)	σ (nb)	$E_{\rm c.m.}$ (GeV)	σ (nb)	$E_{\rm c.m.}$ (GeV)	σ (nb)	$E_{\rm c.m.}$ (GeV)	σ (nb)
1.36–1.38	0.208 ± 0.120	1.96–1.98	0.088 ± 0.035	2.56–2.58	0.111 ± 0.034	3.16–3.18	0.047 ± 0.021
1.38–1.40	0.100 ± 0.089	1.98–2.00	0.098 ± 0.038	2.58–2.60	0.120 ± 0.036	3.18–3.20	0.005 ± 0.010
1.40–1.42	0.042 ± 0.059	2.00–2.02	0.092 ± 0.046	2.60–2.62	0.040 ± 0.025	3.20–3.24	0.016 ± 0.010
1.42–1.44	0.241 ± 0.092	2.02–2.04	0.194 ± 0.052	2.62–2.64	0.028 ± 0.018	3.24–3.28	0.031 ± 0.012
1.44–1.46	0.193 ± 0.091	2.04–2.06	0.120 ± 0.051	2.64–2.66	0.079 ± 0.028	3.28–3.32	0.007 ± 0.008
1.46–1.48	0.370 ± 0.093	2.06–2.08	0.212 ± 0.055	2.66–2.68	0.056 ± 0.025	3.32–3.36	0.025 ± 0.011
1.48–1.50	0.688 ± 0.122	2.08–2.10	0.084 ± 0.038	2.68–2.70	0.067 ± 0.026	3.36–3.40	0.010 ± 0.007
1.50–1.52	0.385 ± 0.092	2.10–2.12	0.271 ± 0.060	2.70–2.72	0.053 ± 0.025	3.40–3.44	0.007 ± 0.008
1.52–1.54	0.485 ± 0.102	2.12–2.14	0.154 ± 0.045	2.72–2.74	0.017 ± 0.020	3.44–3.48	0.002 ± 0.007
1.54–1.56	0.610 ± 0.113	2.14–2.16	0.204 ± 0.056	2.74–2.76	0.040 ± 0.023	3.48–3.52	0.012 ± 0.008
1.56–1.58	0.556 ± 0.109	2.16–2.18	0.191 ± 0.051	2.76–2.78	0.026 ± 0.026	3.52–3.56	0.013 ± 0.008
1.58–1.60	0.911 ± 0.130	2.18–2.20	0.165 ± 0.051	2.78–2.80	0.015 ± 0.020	3.56–3.62	0.006 ± 0.005
1.60–1.62	1.030 ± 0.132	2.20–2.22	0.128 ± 0.049	2.80–2.82	0.046 ± 0.025	3.62–3.68	0.006 ± 0.006
1.62–1.64	0.882 ± 0.127	2.22–2.24	0.185 ± 0.050	2.82–2.84	0.025 ± 0.017	3.68–3.74	0.015 ± 0.007
1.64–1.66	0.767 ± 0.116	2.24–2.26	0.111 ± 0.041	2.84–2.86	0.070 ± 0.027	3.74–3.80	0.013 ± 0.006
1.66–1.68	0.749 ± 0.114	2.26–2.28	0.262 ± 0.056	2.86–2.88	0.050 ± 0.024	3.80–3.86	0.004 ± 0.005
1.68–1.70	0.413 ± 0.082	2.28–2.30	0.107 ± 0.037	2.88–2.90	0.060 ± 0.025	3.86–3.92	0.018 ± 0.007
1.70–1.72	0.296 ± 0.071	2.30–2.32	0.156 ± 0.049	2.90–2.92	0.078 ± 0.028	3.92–3.98	0.005 ± 0.004
1.72–1.74	0.093 ± 0.046	2.32–2.34	0.141 ± 0.041	2.92–2.94	0.044 ± 0.020	3.98–4.04	0.003 ± 0.004
1.74–1.76	0.116 ± 0.046	2.34–2.36	0.128 ± 0.040	2.94–2.96	0.042 ± 0.021	4.04–4.10	0.002 ± 0.005
1.76–1.78	0.073 ± 0.038	2.36–2.38	0.114 ± 0.038	2.96–2.98	0.079 ± 0.027	4.10–4.16	0.005 ± 0.004
1.78–1.80	0.037 ± 0.033	2.38–2.40	0.161 ± 0.043	2.98–3.00	0.025 ± 0.020	4.16–4.24	0.002 ± 0.003
1.80–1.82	0.035 ± 0.033	2.40–2.42	0.060 ± 0.028	3.00–3.02	0.075 ± 0.027	4.24–4.32	0.012 ± 0.005
1.82–1.84	0.066 ± 0.032	2.42–2.44	0.107 ± 0.035	3.02–3.04	0.040 ± 0.020	4.32–4.40	0.008 ± 0.004
1.84–1.86	0.042 ± 0.036	2.44–2.46	0.078 ± 0.032	3.04–3.06	0.052 ± 0.021	4.40–4.48	0.006 ± 0.004
1.86–1.88	0.029 ± 0.033	2.46–2.48	0.005 ± 0.025	3.06–3.08	0.121 ± 0.036	4.48–4.56	0.005 ± 0.003
1.88–1.90	0.053 ± 0.033	2.48–2.50	0.034 ± 0.023	3.08–3.10	0.862 ± 0.088	4.56–4.64	0.002 ± 0.002
1.90–1.92	0.084 ± 0.037	2.50–2.52	0.063 ± 0.033	3.10–3.12	0.698 ± 0.079	4.64–4.72	0.001 ± 0.002
1.92–1.94	0.036 ± 0.024	2.52–2.54	0.110 ± 0.038	3.12–3.14	0.049 ± 0.024		
1.94–1.96	0.164 ± 0.048	2.54–2.56	0.058 ± 0.026	3.14–3.16	0.039 ± 0.019		

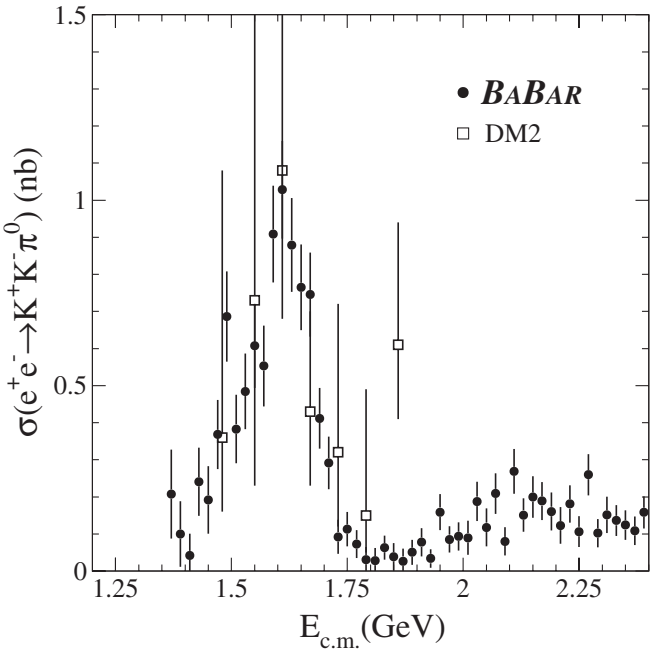

FIG. 12. Comparison of the $e^+e^- \to K^+K^-\pi^0$ cross section measured in *BABAR* with previous experiments.

TABLE IV. Summary of corrections and systematic errors applied to the $e^+e^- \to K^+K^-\pi^0$ cross section measurement.

Source	Correction	Systematic error
ISR luminosity	—	3.0%
$q\bar{q}$ background	—	2.5%
ISR background	—	2.0%
Track reconstruction efficiency	+1.6%	1.0%
PID efficiency	—	2.0%
π^0 reconstruction efficiency	+3.0%	3.0%
MC model	—	3.0%
Total	+4.6%	6.5%

+4.6%, while the estimated total systematic error is ±6.5%.

VI. THE DALITZ PLOT ANALYSIS FOR $K^0_S K^\pm \pi^\mp$ AND $K^+K^-\pi^0$ CHANNELS

Figures 13 and 14 show the Dalitz plot at c.m. energies below 3.1 GeV for the $K^+K^-\pi^0$ and $K^0_S K^\pm \pi^\mp$ final states, respectively. We observe that the intermediate states $KK^*(892)$ and $KK_2^*(1430)$, carrying the allowed combinations of quantum numbers, give the main contributions to the $KK\pi$ production, while $KK_1^*(1410)$ contributes only weakly due to the small value of $\Gamma(K_1^*(1410) \to K\pi)$.

The final $K^0_S K^\pm \pi^\mp$ state can be produced through the intermediate states $K^{*\pm}(892)K^\mp$ or $K_2^{*\pm}(1430)K^\mp$, and we expect a Dalitz plot with a symmetric population density with respect to the exchange $K^+\pi^0(K^{*+}) \leftrightarrow K^-\pi^0(K^{*-})$, see Fig. 13.

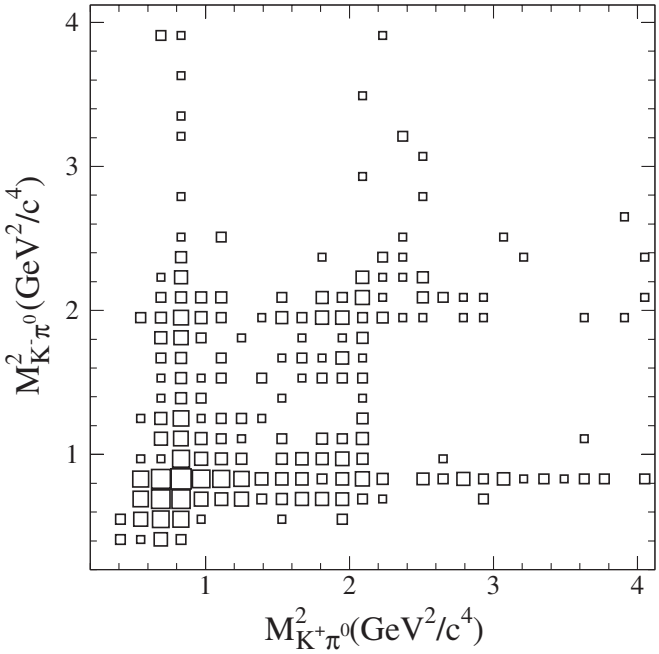

FIG. 13. The Dalitz plot distribution for the $K^+K^-\pi^0$ final state.

The final state $K^0_S K^\pm \pi^\mp$ is obtained via the decays of $K^{*\pm}(892)K^\mp$ and $K^{*0}(892)K^0_S$, or $K_2^{*\pm}(1430)K^\mp$ and $K_2^{*0}(1430)K^0_S$, i.e., both charged $K^{*\pm}(K^0_S\pi^\pm)$ and neutral $K^{*0}(K^\mp\pi^\pm)$ can be produced. The population density of the Dalitz plot is expected to be asymmetric in this case. This effect is clearly seen in Fig. 14.

A detailed explanation of the analysis techniques and the results obtained is given in the following subsection.

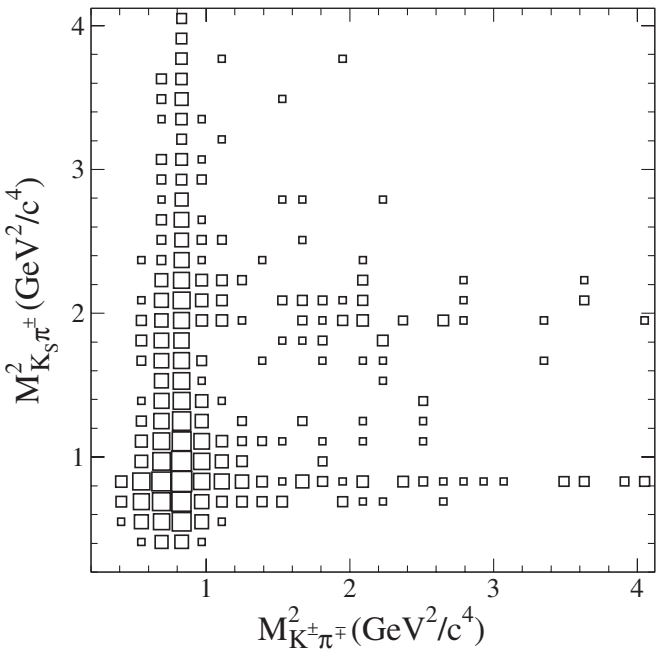

FIG. 14. The Dalitz plot distribution for the $K^0_S K^\pm \pi^\mp$ final state.

TABLE V. Values of the Zemach tensor $\vec{T}_{K^*}$ [20] in the two cases under consideration.

Meson K^*	J^P	L	$\vec{T}_{K^*}(\vec{p}_1 - \vec{p}_2, \vec{p}_3)$
$K^*(892)$	1^-	P	$(\vec{p}_1 - \vec{p}_2) \times \vec{p}_3$
$K_2^*(1430)$	2^+	D	$[(\vec{p}_1 - \vec{p}_2) \cdot \vec{p}_3](\vec{p}_1 - \vec{p}_2) \times \vec{p}_3$

A. The Dalitz method

The Dalitz plot population has been fit assuming KK^* two-body processes as intermediate states and a continuum contribution coming from tails of resonances coupled with KK^*, but lying below their production threshold [20] (see Sec. X). The density function is written in terms of 3-vector isospin amplitudes $\vec{A}_{I,K^*}$, that, in turn, are products of a Breit Wigner distribution (BW), the K^* propagator, and angular distribution probabilities, described by Zemach tensors [21]. In this case, since the spectator particle is always a pseudoscalar meson (the kaon), the Zemach tensors are simply 3-vectors and the amplitudes are

$$\vec{A}_{I,K^*} = C_{I,K^*}\vec{T}_{K^*}(\vec{p}_\pi - \vec{p}_K, \vec{p}_{\bar{K}}) \cdot BW_{K^*}[(p_\pi + p_K)^2] + C_{I,\bar{K}^*}\vec{T}_{\bar{K}^*}(\vec{p}_{\bar{K}} - \vec{p}_\pi, \vec{p}_K) \cdot BW_{\bar{K}^*}[(p_{\bar{K}} + p_\pi)^2], \quad (3)$$

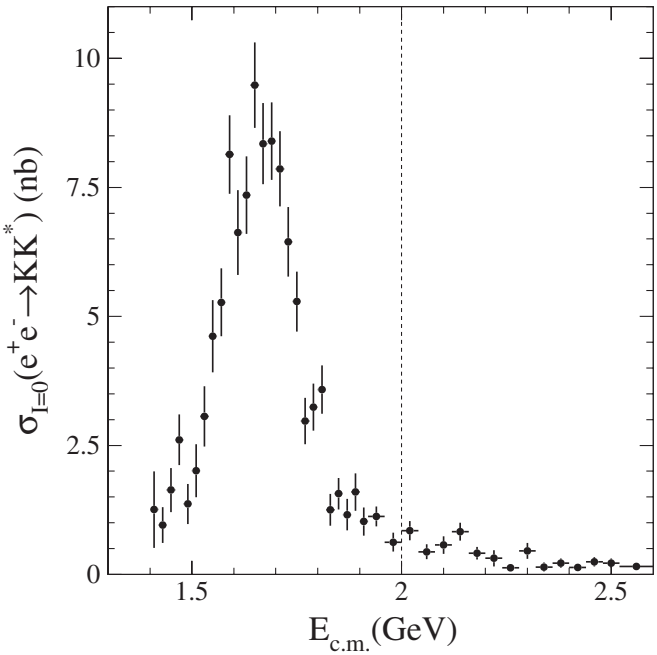

FIG. 16. Isoscalar component of the cross section for the process $e^+e^- \to K^*(892)K$. The vertical line indicates the separation between the two regions used in the analysis.

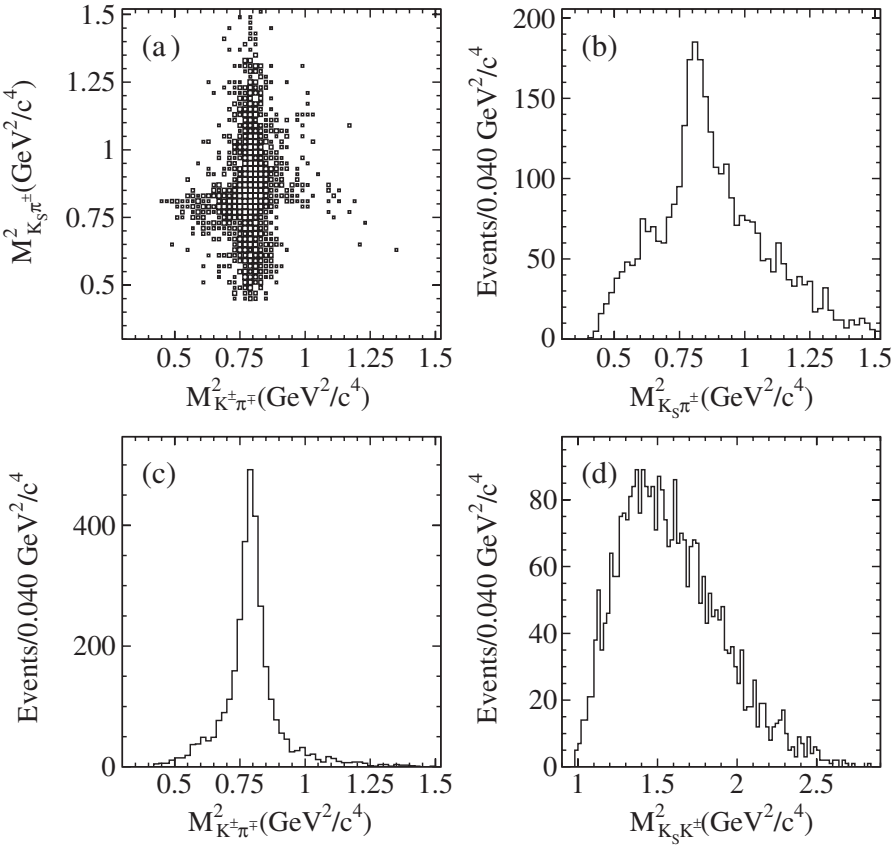

FIG. 15. (a) Dalitz plot distributions for $K^0_S K^\pm\pi^\mp$ events with an invariant mass $M_{K^0_S K\pi} < 2.0$ GeV/c^2. (b) $K^0_S\pi^\pm$ projection, with the broad charged $K^*(892)$ peak, (c) $K^\pm\pi^\mp$ projection, with the narrow neutral $K^*(892)$ peak. (d) $K^0_S K^\pm$ projection.

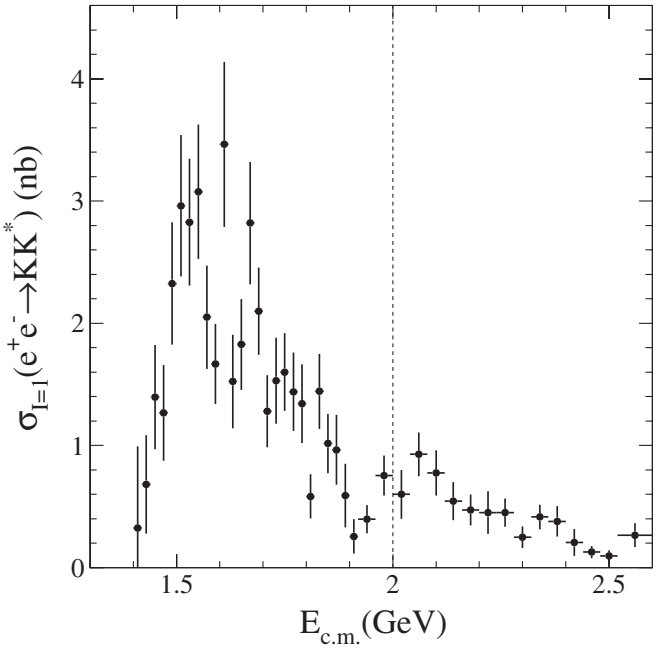

FIG. 17. Isovector component of the cross section for the process $e^+e^- \to K^*(892)K$. The vertical line indicates the separation between the two regions used in the analysis.

where p_α is the 4-momentum of the generic final meson α and $\vec{T}_{K^*}$ is the Zemach tensor related to the K^*. The two terms of Eq. (3) correspond to the two possible $K\pi$ and $\bar{K}\pi$ combinations in which the K^* and $\bar{K}^*$ can exist. The coefficient C^I_α, which accounts for the total isospin I and the charge of the intermediate kaon α, has the form

$$C_{I,K^*} = \begin{cases} (-1)^I & \text{for charged } K^* \\ 1 & \text{for neutral } K^* \end{cases}. \tag{4}$$

The Zemach tensors for $K^*(892)$ and the $K^*_2(1430)$ are shown in Table V.

The Dalitz density has been fit in each bin of $E_{c.m.}$ with the function

$$\mathcal{D}[(p_\pi + p_K)^2, (p_{\bar{K}} + p_\pi)^2, E_{c.m.}] = \sum_{\substack{I,I'=0,1 \\ K^*,K^{*\prime}=K^*(892),K^*_2(1430)}} f_{I,K^*} f^*_{I',K^{*\prime}} \vec{A}_{I,K^*} \cdot \vec{A}^*_{I',K^{*\prime}}, \tag{5}$$

where the $\vec{A}_{I,K^*}$ are the known amplitudes of Eq. (3), which depend on the K^* ($K\pi$) invariant mass and the total energy $E_{c.m.}$, and the complex coefficients f_{I,K^*}, depending only on $E_{c.m.}$, and proportional to the isospin component of the corresponding K^*K channel, are the free parameters. The complex values of the f_{I,K^*} parameters have been used to extract moduli and relative phase of the isospin components. The analysis described in the following applies only to the $K^0_S K^\pm \pi^\mp$ Dalitz plot, since only in this case, with both charged and neutral K^* contributing, we can separately extract the isoscalar and isovector components. Because the $KK^*(892)$ and $KK^*_2(1430)$ represent the dominant contribution to the $KK\pi$ production at c.m. energies below and above 2.0 GeV, respectively, these two regions have been considered separately.

Figure 15 shows, in the low-energy region, the $K^0_S K^\pm \pi^\mp$ Dalitz plot and the three possible projections. The dominance of the $K^*(892)$ in each $K\pi$ channel appears evident. As a result, in the following we will consider the process $e^+e^- \to K^*(892)K$ as the dominant one. The different shapes observed for the charged [Fig. 15(b)] and neutral $K^*(892)$ [Fig. 15(c)], are due to interference effects between the isoscalar and isovector components (see Sec. X A).

Figures 16 and 17 show the isoscalar and isovector cross sections; numerical values are reported in Tables VI and VII, respectively. Figure 18 shows the relative phase between the two amplitudes. In addition to the errors reported in Table I we must consider the 15% systematic uncertainty associated with the Dalitz plot-fit procedure. This quantity

TABLE VI. Isoscalar component of the cross section as a function of $E_{c.m.}$ for the process $e^+e^- \to K^*(892)K$. Errors are statistical only.

$E_{c.m.}$ (GeV)	σ (nb)	$E_{c.m.}$ (GeV)	σ (nb)	$E_{c.m.}$ (GeV)	σ (nb)	$E_{c.m.}$ (GeV)	σ (nb)
1.40–1.42	1.26 ± 0.75	1.66–1.68	8.34 ± 0.78	1.92–1.96	1.11 ± 0.18	2.44–2.48	0.24 ± 0.09
1.42–1.44	0.96 ± 0.36	1.68–1.70	8.40 ± 0.75	1.96–2.00	0.63 ± 0.18	2.48–2.52	0.21 ± 0.09
1.44–1.46	1.62 ± 0.42	1.70–1.72	7.86 ± 0.72	2.00–2.04	0.84 ± 0.18	2.52–2.60	0.15 ± 0.06
1.46–1.48	2.61 ± 0.48	1.72–1.74	6.45 ± 0.69	2.04–2.08	0.45 ± 0.15	2.60–2.68	0.18 ± 0.06
1.48–1.50	1.38 ± 0.39	1.74–1.76	5.28 ± 0.57	2.08–2.12	0.57 ± 0.18	2.68–2.76	0.12 ± 0.03
1.50–1.52	2.01 ± 0.51	1.76–1.78	2.97 ± 0.45	2.12–2.16	0.84 ± 0.18	2.76–2.84	0.09 ± 0.03
1.52–1.54	3.06 ± 0.57	1.78–1.80	3.24 ± 0.45	2.16–2.20	0.42 ± 0.12	2.84–2.92	0.09 ± 0.06
1.54–1.56	4.62 ± 0.69	1.80–1.82	3.57 ± 0.48	2.20–2.24	0.30 ± 0.15	2.92–3.00	0.15 ± 0.03
1.56–1.58	5.28 ± 0.66	1.82–1.84	1.26 ± 0.30	2.24–2.28	0.12 ± 0.06	3.00–3.08	0.09 ± 0.03
1.58–1.60	8.13 ± 0.75	1.84–1.86	1.56 ± 0.30	2.28–2.32	0.45 ± 0.15	3.08–3.16	1.95 ± 0.15
1.60–1.62	6.63 ± 0.81	1.86–1.88	1.17 ± 0.30	2.32–2.36	0.15 ± 0.09		
1.62–1.64	7.35 ± 0.75	1.88–1.90	1.59 ± 0.36	2.36–2.40	0.21 ± 0.09		
1.64–1.66	9.48 ± 0.84	1.90–1.92	1.02 ± 0.27	2.40–2.44	0.15 ± 0.06		

TABLE VII. Isovector component of the cross section as a function of $E_{\rm c.m.}$ for the process $e^+e^- \to K^*(892)K$. Errors are statistical only.

$E_{\rm c.m.}$ (GeV)	σ (nb)	$E_{\rm c.m.}$ (GeV)	σ (nb)	$E_{\rm c.m.}$ (GeV)	σ (nb)	$E_{\rm c.m.}$ (GeV)	σ (nb)
1.40–1.42	0.32 ± 0.67	1.64–1.66	1.83 ± 0.37	1.88–1.90	0.59 ± 0.26	2.28–2.32	0.25 ± 0.09
1.42–1.44	0.68 ± 0.40	1.66–1.68	2.82 ± 0.50	1.90–1.92	0.26 ± 0.14	2.32–2.36	0.41 ± 0.10
1.44–1.46	1.40 ± 0.43	1.68–1.70	2.10 ± 0.36	1.92–1.94	0.51 ± 0.17	2.36–2.40	0.38 ± 0.13
1.46–1.48	1.27 ± 0.39	1.70–1.72	1.28 ± 0.30	1.92–1.96	0.40 ± 0.12	2.40–2.44	0.21 ± 0.11
1.48–1.50	2.33 ± 0.50	1.72–1.74	1.53 ± 0.35	1.96–2.00	0.75 ± 0.16	2.44–2.48	0.13 ± 0.05
1.50–1.52	2.96 ± 0.58	1.74–1.76	1.60 ± 0.32	2.00–2.04	0.60 ± 0.20	2.48–2.52	0.10 ± 0.05
1.52–1.54	2.83 ± 0.52	1.76–1.78	1.44 ± 0.32	2.04–2.08	0.93 ± 0.18	2.52–2.60	0.27 ± 0.10
1.54–1.56	3.08 ± 0.55	1.78–1.80	1.34 ± 0.32	2.08–2.12	0.78 ± 0.18	2.60–2.68	0.05 ± 0.03
1.56–1.58	2.05 ± 0.42	1.80–1.82	0.58 ± 0.18	2.12–2.16	0.55 ± 0.16	2.68–2.76	0.11 ± 0.04
1.58–1.60	1.67 ± 0.33	1.82–1.84	1.44 ± 0.31	2.16–2.20	0.47 ± 0.13	2.76–2.84	0.11 ± 0.03
1.60–1.62	3.46 ± 0.68	1.84–1.86	1.02 ± 0.24	2.20–2.24	0.45 ± 0.17	2.84–2.92	0.04 ± 0.01
1.62–1.64	1.52 ± 0.38	1.86–1.88	0.96 ± 0.29	2.24–2.28	0.45 ± 0.12	2.92–3.08	0.03 ± 0.01

has been evaluated by studying the effects of different parametrizations for the *BW* distributions which describe the intermediate K^* resonances in the amplitudes of Eq. (3). The isoscalar contribution, see Fig. 16, is dominant with respect to the isovector (Fig. 17) and clearly shows a resonant behavior. Moreover, the isovector cross section seems to be compatible with a pure phase space shape. However, using the complete information, including the relative phase, shown in Fig. 18, we also find that the isovector component has a resonant structure (for details see Sec. X A).

Figure 19 shows the Dalitz plot and the projections obtained in the c.m. energy region above 2.0 GeV. In this case, in addition to the $KK^*(892)$, we have evidence that the $KK_2^*(1430)$ intermediate state also contributes. In particular, as theoretically predicted [22], we observe that while the neutral $K^*(892)$ dominates the $K^\pm\pi^\mp$ projection [Fig. 19(c)], the charged $K_2^*(1430)$ is the main contribution in the $K_S^0\pi^\pm$ projection [Fig. 19(b)]. This can be interpreted as a different spatial structure of these mesons: $K^*(892)$ is a vector, while $K_2^*(1430)$ is a tensor. The Dalitz plot analysis in this energy range is performed with four isospin amplitudes, an isoscalar, and an isovector component for each intermediate two-body channel. Figures 20(a) and 20(b) show the isoscalar and isovector components of the $K_2^*(1430)K$ channel. The corresponding values are reported in Tables VIII and IX, respectively. The structure observed at $E_{\rm c.m.} \simeq 2.1$ GeV in the isoscalar and $E_{\rm c.m.} \simeq 2.25$ GeV in the isovector components may be interpreted as pure threshold effects. Indeed, the transition form factors, obtained by taking the square root of the cross sections divided by the appropriate phase space (a pseudoscalar and a tensor meson in the final state), have a steep yet smooth behavior, as shown in Fig. 21. The simplest interpretation calls for transition form factors that collect the main contributions from low-energy resonances lying below threshold. Further study and higher statistics would help to clarify this item.

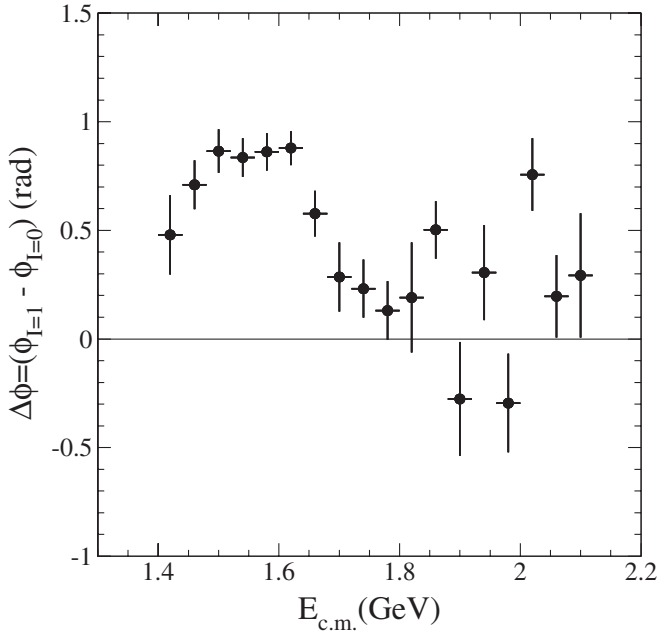

FIG. 18. Relative phase between the isoscalar and isovector component of the $e^+e^- \to K^*(892)K$ cross section.

VII. THE J/ψ REGION

Clean J/ψ signals are observed in almost all the final states under study, from which we extract the corresponding decay rates. Figure 22(a) shows the inclusive distribution in the J/ψ mass region for the $K_S^0K^\pm\pi^\mp$ data sample. A fit with a Gaussian for the J/ψ peak and a linear function for the continuum gives $\sigma(M_{K_S^0K\pi}) = 6.5$ MeV$/c^2$ and less than 1 MeV$/c^2$ difference from the PDG [17] value for the J/ψ mass. To account also for possible radiative or experimental effects we determine the yields under the J/ψ peak by fitting with a double-Gaussian. As shown by the analysis, the $e^+e^- \to KK\pi$ reactions proceed

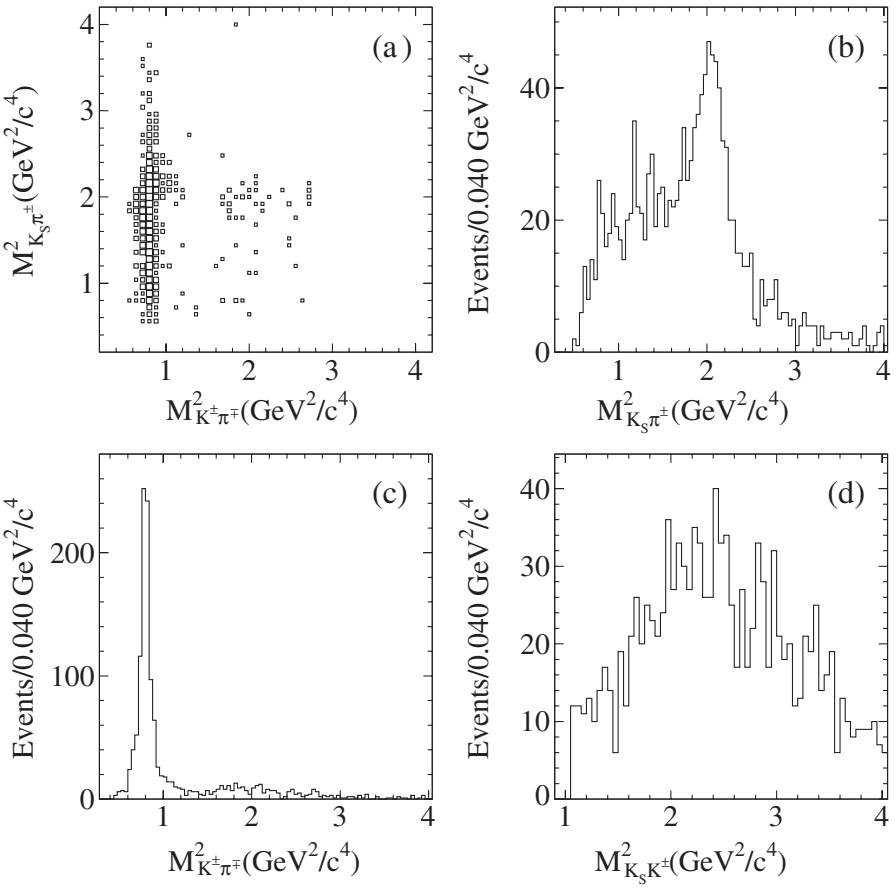

FIG. 19. (a) Dalitz plot distributions for $K^0_S K^\pm \pi^\mp$ events with an invariant mass $M_{K^0_S K\pi} > 2.0$ GeV/c^2. (b) $K^0_S\pi^\pm$ projection, with the broad charged $K^*_2(1430)$ peak. (c) $K^\pm\pi^\mp$ projection, with the narrow neutral $K^*(892)$ peak. (d) $K^0_S K^\pm$ projection.

mainly through the formation of the intermediate $KK^*(892)$ state. We could therefore extract the $J/\psi \to K^*(892)K$ decay rates, where the $K^*(892)$ is charged ($K^{*\pm}(892) \to K^\pm\pi^0$) for the $K^+K^-\pi^0$ final state and neutral $K^{*0}(892) \to K^\pm\pi^\mp$ or charged ($K^{*\pm}(892) \to K^0_S\pi^\pm$) for the $K^0_S K^\pm\pi^\mp$ final state. In order to isolate the different $K^*(892)$ contributions, we require $E_K > 1.4$ GeV in the $KK\pi$ c.m. frame for the kaon not coming from the $K^*(892)$ decay, as expected for a two-body J/ψ decay. A check of the Dalitz plot provides an estimate of the residual contamination from wrong $K\pi$ combinations, which is found to be less than 3.0%. From the fit to the mass distributions obtained for the different $K^*(892)K$ final states, shown in Figs. 22(b)–22(d), we derive the number of events reported

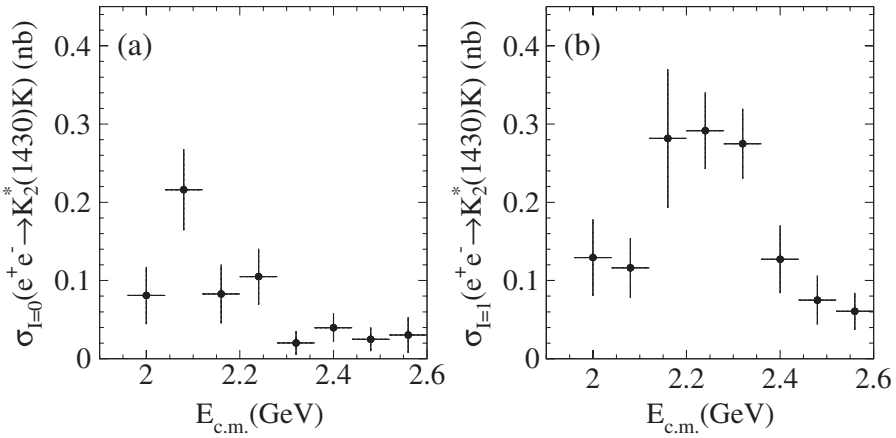

FIG. 20. Isoscalar (a) and isovector (b) components of the cross section for the process $e^+e^- \to K^*_2(1430)K$.

TABLE VIII. Isoscalar component of the cross section as a function of $E_{\rm c.m.}$ for the process $e^+e^- \to K_2^*(1430)K$. Errors are statistical only.

$E_{\rm c.m.}$ (GeV)	σ (nb)	$E_{\rm c.m.}$ (GeV)	σ (nb)	$E_{\rm c.m.}$ (GeV)	σ (nb)	$E_{\rm c.m.}$ (GeV)	σ (nb)
1.92–1.96	0.069 ± 0.036	2.16–2.20	0.252 ± 0.100	2.40–2.44	0.014 ± 0.007	2.76–2.84	0.009 ± 0.009
1.96–2.00	0.048 ± 0.033	2.20–2.24	0.115 ± 0.060	2.44–2.48	0.128 ± 0.066	2.84–2.92	0.022 ± 0.012
2.00–2.04	0.083 ± 0.051	2.24–2.28	0.059 ± 0.037	2.48–2.52	0.008 ± 0.004	2.92–3.00	0.065 ± 0.019
2.04–2.08	0.261 ± 0.088	2.28–2.32	0.034 ± 0.023	2.52–2.60	0.030 ± 0.031	3.00–3.08	0.044 ± 0.025
2.08–2.12	0.172 ± 0.089	2.32–2.36	0.045 ± 0.028	2.60–2.68	0.012 ± 0.012		
2.12–2.16	0.018 ± 0.018	2.36–2.40	0.063 ± 0.055	2.68–2.76	0.003 ± 0.003		

TABLE IX. Isovector component of the cross section as a function of $E_{\rm c.m.}$ for the process $e^+e^- \to K_2^*(1430)K$. Errors are statistical only.

$E_{\rm c.m.}$ (GeV)	σ (nb)	$E_{\rm c.m.}$ (GeV)	σ (nb)	$E_{\rm c.m.}$ (GeV)	σ (nb)	$E_{\rm c.m.}$ (GeV)	σ (nb)
1.96–2.00	0.10 ± 0.07	2.20–2.24	0.21 ± 0.07	2.44–2.48	0.06 ± 0.03	2.84–2.92	0.04 ± 0.02
2.00–2.04	0.23 ± 0.09	2.24–2.28	0.42 ± 0.10	2.48–2.52	0.02 ± 0.01	2.92–3.00	0.05 ± 0.02
2.04–2.08	0.08 ± 0.05	2.28–2.32	0.32 ± 0.11	2.52–2.60	0.06 ± 0.03	3.00–3.08	0.03 ± 0.01
2.08–2.12	0.19 ± 0.09	2.32–2.36	0.15 ± 0.07	2.60–2.68	0.13 ± 0.03		
2.12–2.16	0.33 ± 0.10	2.36–2.40	0.09 ± 0.05	2.68–2.76	0.08 ± 0.03		
2.16–2.20	0.27 ± 0.10	2.40–2.44	0.18 ± 0.07	2.76–2.84	0.03 ± 0.02		

in Table X, together with the corresponding J/ψ branching fractions multiplied by the $J/\psi \to e^+e^-$ width. The latter quantity has been obtained through

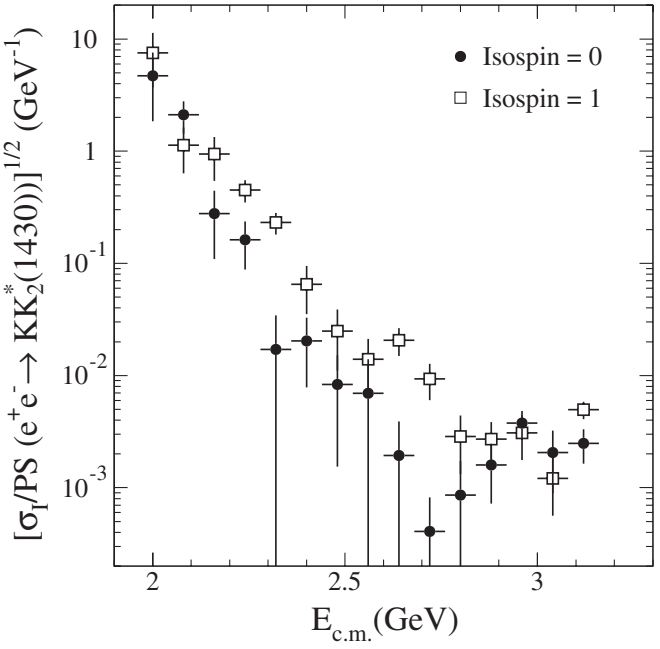

FIG. 21. The isospin amplitudes (defined as the square root of the isospin components divided by the phase space) for the $K_S^0K^\pm\pi^\mp$ channel, obtained by fitting the Dalitz plot in the region $E_{\rm c.m.} > 2.0$ GeV, in the case of $K_2^*(1430)K$ intermediate state.

$$\mathcal{B}_f^{J/\psi} \cdot \Gamma_{ee}^{J/\psi} = \frac{N(J/\psi \to f) \cdot m_{J/\psi}^2}{6\pi^2 \cdot d\mathcal{L}/dE \cdot \epsilon \cdot C}, \qquad (6)$$

where $\mathcal{B}_f^{J/\psi}$ is the branching fraction for $J/\psi \to f$, $d\mathcal{L}/dE = 65.6\ \text{nb}^{-1}/\text{MeV}$ is the ISR luminosity integrated at the J/ψ mass, ϵ is the detection efficiency obtained from simulation, and $C \equiv (hc/2\pi)^2 = 3.894 \times 10^{11}\ \text{nb}\,\text{MeV}^2$ is a conversion constant. The systematic errors have been estimated by considering, in addition to the values reported in Tables I and IV, the statistical error on the reconstruction efficiency. Assuming the world average value of the $J/\psi \to e^+e^-$ width, $\Gamma_{ee} = 5.55 \pm 0.14$ keV [17], we extract the decay rates shown in the last column of Table X. Here and in the following the first uncertainty reported is statistical and the second is systematic. From these results and the known $K^*(892)$ decay rates, we can derive the $J/\psi \to K^{*0}(892)\bar{K}^0$, $K^{*+}(892)K^-$ branching fractions, summarized in Table XI.

VIII. THE $\phi\pi^0$ FINAL STATE

The event selection for $\phi\pi^0$ production closely follows the procedure described for $K^+K^-\pi^0$ with nonresonant K^+K^- pairs. We tighten a few cuts in order to remove random photon combinations that could fake a π^0. In particular we lowered to 300 MeV the cut on the additional detected neutral energy, and we require that the direction of the observed ISR photon matches the 1C fit prediction within 12 mrad.

Figure 23 shows the K^+K^- mass, M_{KK}, versus the $\gamma\gamma$ mass, $M_{\gamma\gamma}$. The plot is divided into nine equally sized

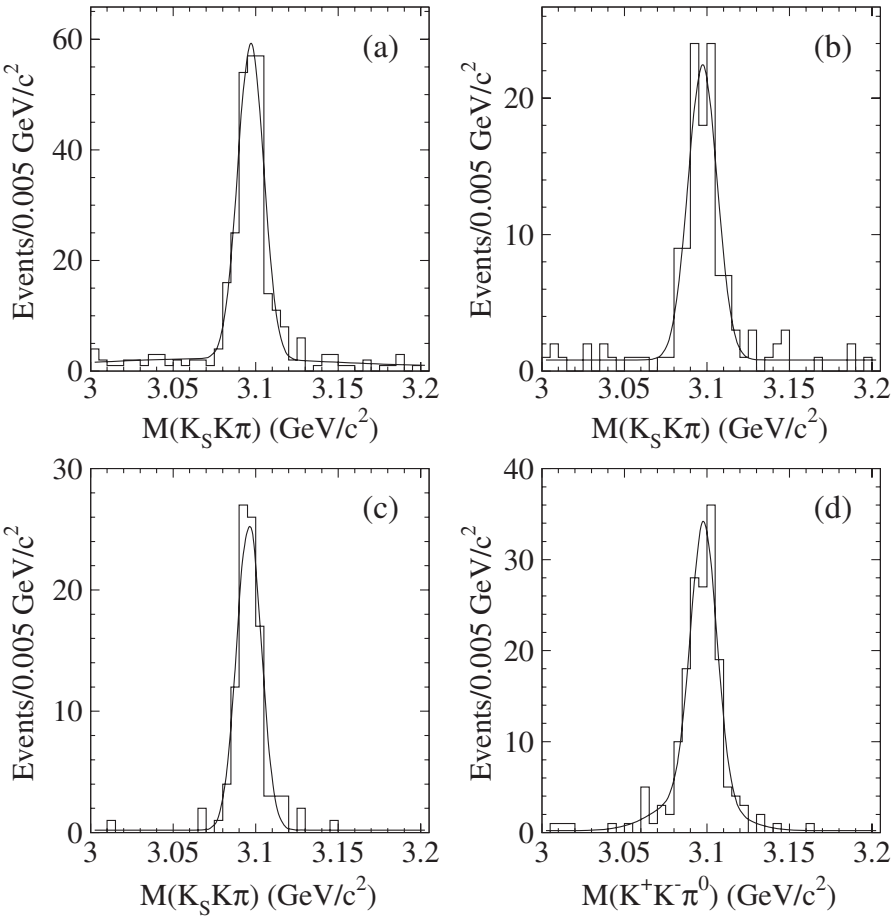

FIG. 22. (a) $K^0_S K^\pm \pi^\mp$ mass distribution in the J/ψ mass region. (b–d) Mass distributions of selected events for: (b) $K^{*0}(892)K^0_S(K^{*0}(892) \to K^\pm \pi^\mp)$; (c) $K^{*\pm}(892)K^\mp(K^{*\pm}(892) \to K^0_S \pi^\pm)$; and (d) $K^{*\pm}(892)K^\mp(K^{*\pm}(892) \to K^\pm \pi^0)$. The curves represent the fits obtained using a sum of two Gaussians and a linear function.

regions, with the central one, which corresponds to $1.010 < M_{KK} < 1.030$ GeV$/c^2$ and $0.110 < M_{\gamma\gamma} < 0.160$ GeV$/c^2$, being the signal region. We extract the number of signal S and background B events contained in the central cell, by solving the following linear equation system:

$$N_0 = S + B = 76, \quad N_1 = 0.135 \cdot S + 2 \cdot B = 51, \quad (7)$$

where N_0 and N_1 are the yields in the central cell and the sum of yields in adjacent cells (i.e., the cells numbered as 2, 4, 6, and 8 in Fig. 23), respectively. The fractions of signal events contained in the central and adjacent cells have been determined from MC simulation, while the factor of 2 multiplying B in the second equation is a consequence of the fact that the background is linear with respect to both $\gamma\gamma$ and KK masses. We find 54 signal and 22 background events.

TABLE X. Branching ratios of the $J/\psi \to KK\pi$ decays. The value of $\Gamma^{J/\psi}_{ee}$ is taken from Ref. [17].

Final state, f	Yield	$\mathcal{B}^{J/\psi}_f \Gamma^{J/\psi}_{ee}$ (eV)	$\mathcal{B}^{J/\psi}_f \cdot 10^3$
$(K^\pm \pi^\mp)K_S$	94 ± 9	$8.85 \pm 0.85 \pm 0.50$	$1.59 \pm 0.16 \pm 0.09$
$(K_S \pi^\pm)K^\mp$	89 ± 9	$8.38 \pm 0.85 \pm 0.50$	$1.51 \pm 0.16 \pm 0.09$
$(K^\pm \pi^0)K^\mp$	155 ± 12	$10.96 \pm 0.85 \pm 0.70$	$1.97 \pm 0.16 \pm 0.13$

TABLE XI. Branching ratios of the $J/\psi \to K^*K$ decay ($\Gamma^{J/\psi}_{ee}$ from Ref. [17] and c.c. stands for charge conjugate).

Final state, f	$\mathcal{B}^{J/\psi}_f \Gamma^{J/\psi}_{ee}$ (eV)	$\mathcal{B}^{J/\psi}_f \cdot 10^3$	$\mathcal{B}^{J/\psi}_f \cdot 10^3$ (Ref. [17])
$(K^{*+}K^-) + \text{c.c.}$	$29.0 \pm 1.7 \pm 1.3$	$5.2 \pm 0.3 \pm 0.3$	5.0 ± 0.4
$(K^{*0}\bar{K}^0) + \text{c.c.}$	$26.6 \pm 2.5 \pm 1.5$	$4.8 \pm 0.5 \pm 0.3$	4.2 ± 0.4

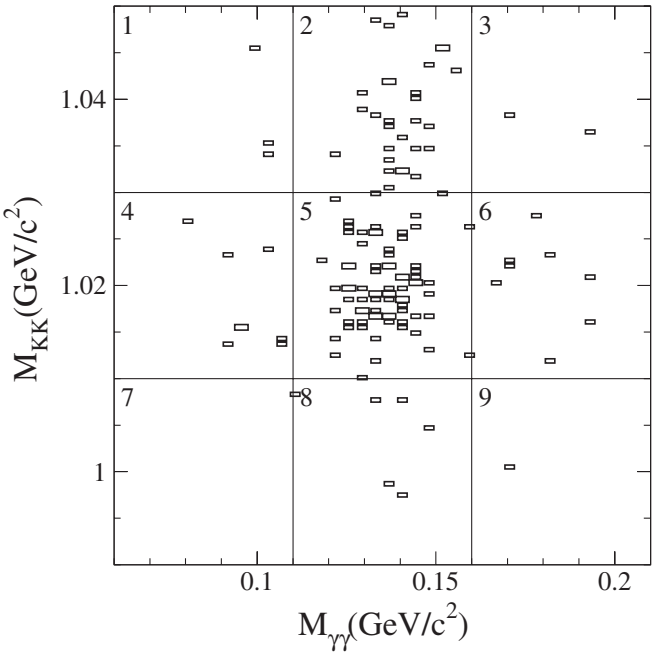

FIG. 23. The 2-dimensional K^+K^-, $\gamma\gamma$ invariant mass distribution around the ϕ and π^0 masses. The central cell identifies the signal region.

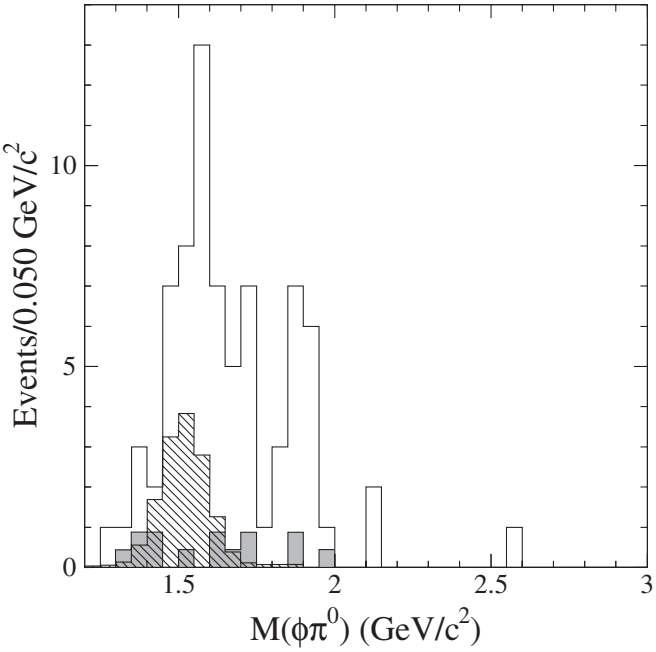

FIG. 25. The invariant mass distribution of the $\phi\pi^0$ system (open histogram). The hatched and gray histograms show the background from non-ϕ $K^+K^-\pi^0$ and from $\gamma\gamma$ combinatorial.

The simulation of specific reactions with a real ϕ and/or π^0 in the final state, like $e^+e^- \to \phi\gamma$, $e^+e^- \to \phi\pi^0\pi^0\gamma$, $e^+e^- \to KK\pi^0\pi^0\gamma$ (nonresonant KK production), and $q\bar{q}$, $\tau\tau$ production from continuum, shows that their contribution is negligible. We can thus conclude that the only sources of background are represented by the $KK\pi^0\gamma$ final state, with nonresonant KK pair, and by a number of ISR processes with a true ϕ and a random $\gamma\gamma$ combination. Figure 24(a) shows the ϕ signal in the K^+K^- invariant mass, after the cut around the π^0 mass is applied; vice versa, Fig. 24(b) shows the π^0 signal once a ϕ is selected. Fitting these distributions with a Gaussian and a linear background we estimate the two background sources to be 15 ± 2 and 7 ± 3 events, respectively.

The mass spectra for the data and the estimated backgrounds are shown in Fig. 25. The mass spectrum for the $KK\pi^0$ background is obtained from the simulated sample, while the spectrum for the other ISR backgrounds is taken directly from the π^0 sidebands.

The $e^+e^- \to \phi\pi^0$ process is simulated considering only $\phi \to K^+K^-$ decays, so that the cross section as a function of the effective c.m. energy is given by

$$\sigma_{e^+e^-\to\phi\pi^0}(E_{\mathrm{c.m.}}) = \frac{dN_{\phi\pi^0\gamma}(E_{\mathrm{c.m.}})}{d\mathcal{L}(E_{\mathrm{c.m.}})\epsilon(E_{\mathrm{c.m.}})\mathcal{B}(\phi \to K^+K^-)}, \tag{8}$$

where $E_{\mathrm{c.m.}}$ is the invariant mass of the $\phi\pi^0$ system;

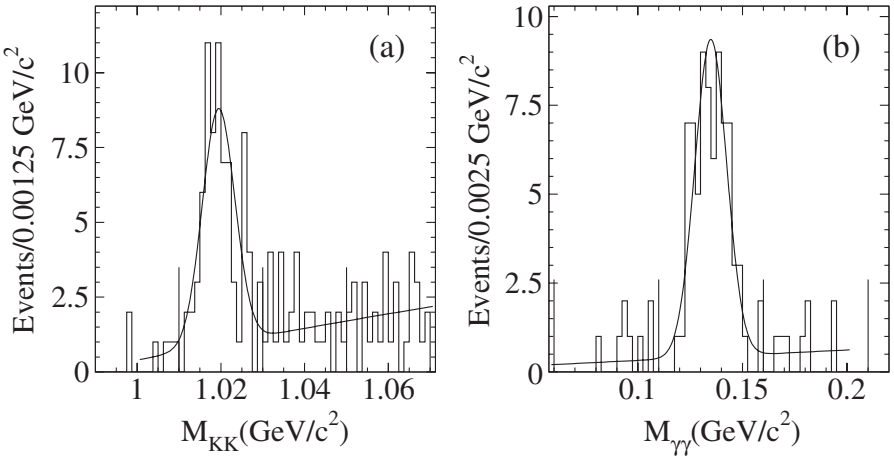

FIG. 24. The K^+K^- (a) and $\gamma\gamma$ (b) invariant mass distributions. Signal and sideband regions are set by vertical lines in the plots.

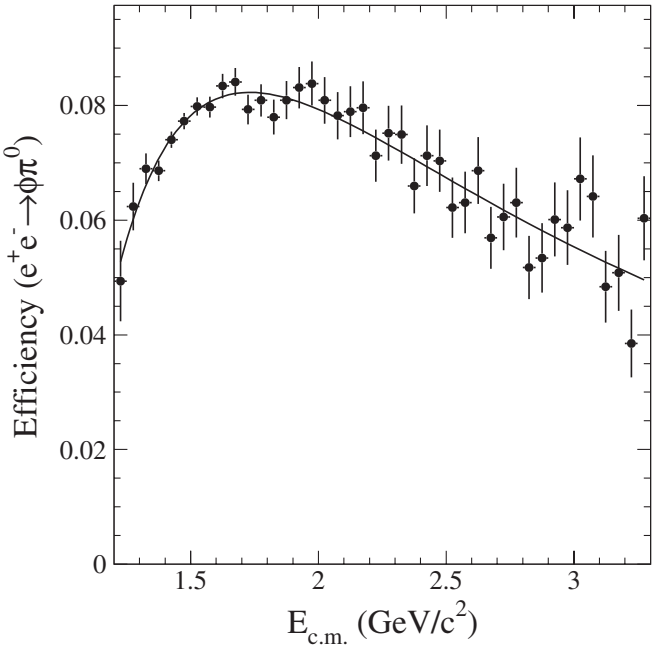

FIG. 26. Detection and reconstruction efficiency as a function of the c.m. energy for the $\phi\pi^0$ final state. The solid line is the result of a fit to the data with the function $a(1-(x/b)^p \cdot e^{\xi(b-x)})$, where $x = E_{\rm c.m.}$.

$dN_{\phi\pi^0\gamma}$ is the number of selected $\phi\pi^0$ events after background subtraction in the interval $dE_{\rm c.m.}$, $\epsilon(E_{\rm c.m.})$ is the detection efficiency obtained from MC simulation (see Fig. 26), and $\mathcal{B}(\phi \to K^+K^-)$ is the world average value of the $\phi \to K^+K^-$ branching fraction [17]. The energy behavior of the cross section is shown in Fig. 27 and reported in Table XII. The cross section has a maximum of about 0.2 nb around 1.6 GeV.

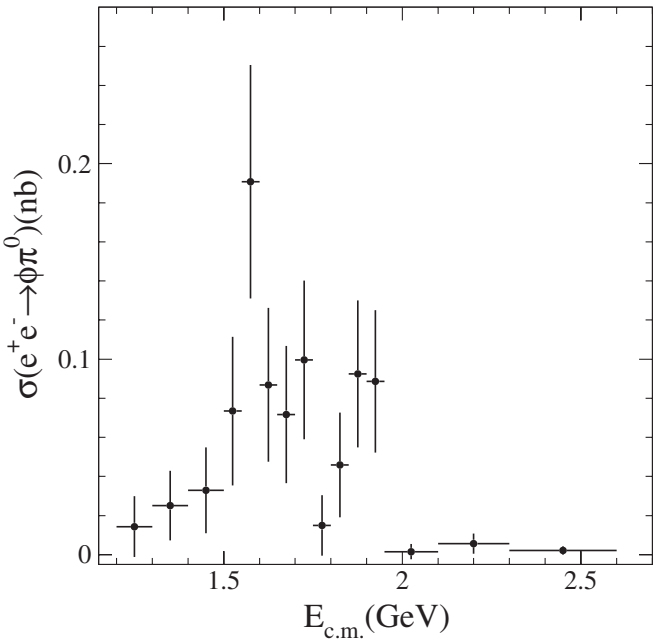

FIG. 27. The $e^+e^- \to \phi\pi^0$ cross section.

The efficiency corrections and the systematic uncertainties which affect the $\phi\pi^0$ cross section measurement are similar to those of the $K^+K^-\pi^0$ reaction. However, the uncertainties on background subtraction are larger, and we have to account also for the 1.2% uncertainty on the $\phi \to K^+K^-$ branching fraction. The total systematic error associated to the cross section measurement is therefore $\pm 8.7\%$.

IX. THE $K^+K^-\eta$ FINAL STATE

We analyze $\phi\eta$ and $K^+K^-\eta$ (with nonresonant K^+K^- pairs) final states separately, selecting samples with an invariant mass of the K^+K^- system below and above 1.045 GeV/c^2: ϕ and NOT-ϕ events, respectively. In both cases, because of the cleanliness of the η signal, no additional cuts on photons or extra neutral energy are required. The K^+K^- and $\gamma\gamma$ invariant mass distributions for selected events are shown in Fig. 28.

A. $e^+e^- \to KK\eta$

Following the same strategy as the analysis described in the previous sections, we select a total of 113 candidate events. We estimate 42 ± 42 $q\bar{q}$ and 15 ± 8 ISR-background events: 56 ± 43 events is then the overall signal yield. Figure 29 shows the $e^+e^- \to K^+K^-\eta$ mass spectrum from production threshold up to 4.3 GeV, together with the estimated backgrounds, while the relative cross section is depicted in Fig. 30 and the results are listed in Table XIII.

The uncertainties on background estimation, in particular, the $q\bar{q}$ contribution, completely dominate the systematic errors, which sum up to about 80%. On the other hand, the J/ψ region is essentially free from any background, as can be seen from the very clean η and J/ψ signals shown in Fig. 31. We select 21 ± 3 $J/\psi \to K^+K^-\eta$ events, from which we measure

$$\mathcal{B}^{J/\psi}_{K^+K^-\eta} \cdot \Gamma^{J/\psi}_{ee} = (4.8 \pm 0.7 \pm 0.3)\ \text{eV}, \qquad (9)$$

and extract the first evaluation of the $J/\psi \to K^+K^-\eta$ branching fraction:

$$\mathcal{B}^{J/\psi}_{K^+K^-\eta} = (8.7 \pm 1.3 \pm 0.7) \times 10^{-4}. \qquad (10)$$

B. $e^+e^- \to \phi\eta$

The extremely clean ϕ signal makes this channel almost background-free. Following the background-subtraction procedure as for the $\phi\pi^0$ final state we get 483 signal and 9 background events. The ϕ signal, once a η is selected, and the η signal, after the ϕ selection, are shown in Fig. 32.

TABLE XII. Measurement of the $e^+e^- \to \phi\pi^0$ cross section as a function of $E_{\rm c.m.}$. Errors are statistical only.

$E_{\rm c.m.}$ (GeV)	σ (nb)	$E_{\rm c.m.}$ (GeV)	σ (nb)	$E_{\rm c.m.}$ (GeV)	σ (nb)	$E_{\rm c.m.}$ (GeV)	σ (nb)
1.20–1.30	0.014 ± 0.016	1.55–1.60	0.191 ± 0.060	1.75–1.80	0.015 ± 0.015	1.95–2.10	0.002 ± 0.004
1.30–1.40	0.025 ± 0.018	1.60–1.65	0.087 ± 0.039	1.80–1.85	0.046 ± 0.027	2.10–2.30	0.006 ± 0.005
1.40–1.50	0.033 ± 0.022	1.65–1.70	0.072 ± 0.035	1.85–1.90	0.093 ± 0.038	2.30–2.60	0.002 ± 0.002
1.50–1.55	0.073 ± 0.038	1.70–1.75	0.100 ± 0.041	1.90–1.95	0.089 ± 0.036		

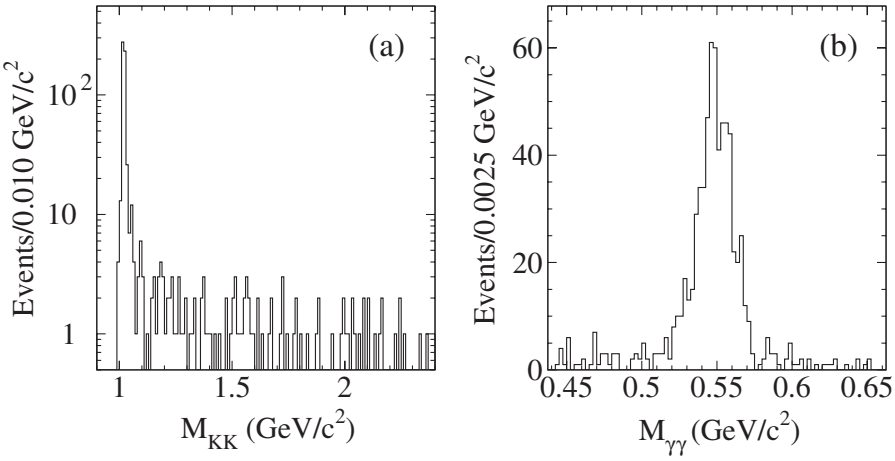

FIG. 28. The K^+K^- (a) and $\gamma\gamma$ (b) invariant mass distributions for selected events.

We simulate several specific reactions with real ϕ and/or η in the final state, namely, different ISR processes and $q\bar{q}$, $\tau\tau$ production, finding no significant contribution. The mass spectrum for signal events is shown in Fig. 33, together with the subtracted distribution for the background events obtained from the side bands.

The efficiency corrections and the systematic uncertainties that affect the $\phi\eta$ cross section measurement are very

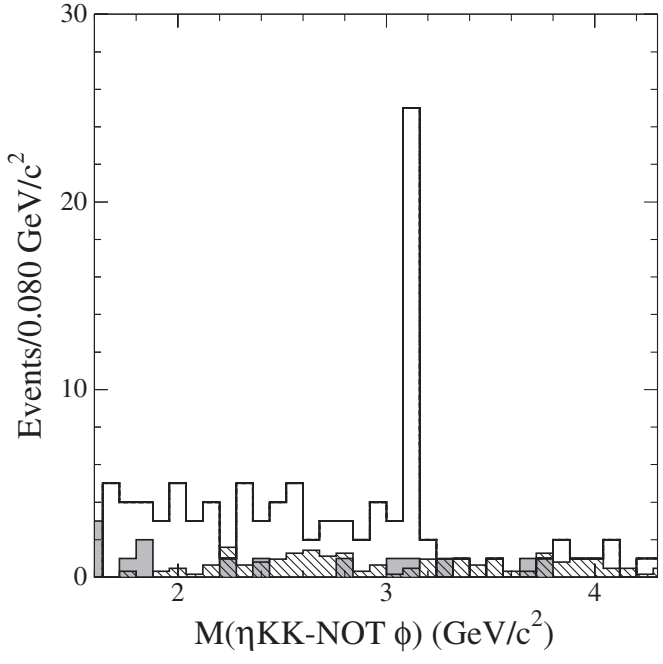

FIG. 29. The invariant mass distribution of the $K^+K^-\eta$ system (open histogram). The hatched and the gray histograms show the $q\bar{q}$ and ISR backgrounds, respectively.

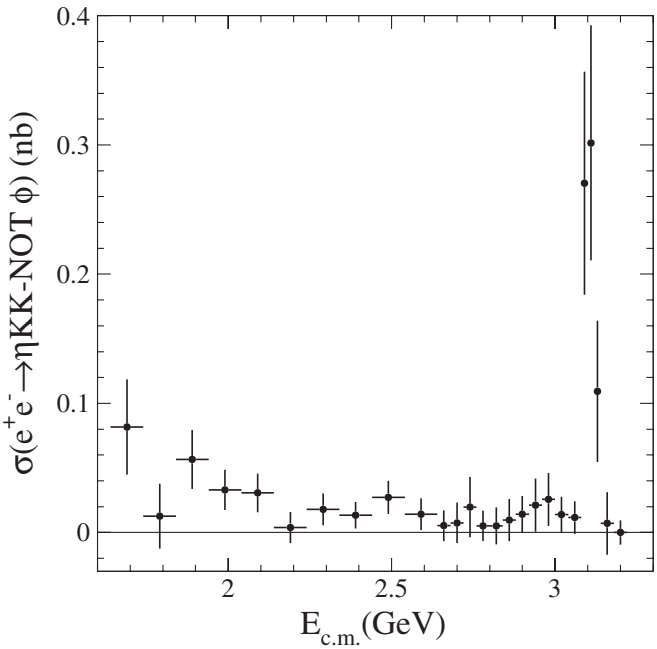

FIG. 30. The $e^+e^- \to K^+K^-\eta$ cross section as a function of c.m. energy.

TABLE XIII. Measurement of the $e^+e^- \to \eta K^+K^-$ (NOT ϕ) cross section as a function of $E_{\text{c.m.}}$. Errors are statistical only.

$E_{\text{c.m.}}$ (GeV)	σ (nb)	$E_{\text{c.m.}}$ (GeV)	σ (nb)	$E_{\text{c.m.}}$ (GeV)	σ (nb)	$E_{\text{c.m.}}$ (GeV)	σ (nb)
1.64–1.74	0.08 ± 0.04	2.24–2.34	0.02 ± 0.01	2.72–2.76	0.02 ± 0.02	2.96–3.00	0.03 ± 0.02
1.74–1.84	0.01 ± 0.03	2.34–2.44	0.01 ± 0.01	2.76–2.80	0.01 ± 0.01	3.00–3.04	0.01 ± 0.01
1.84–1.94	0.06 ± 0.02	2.44–2.54	0.03 ± 0.01	2.80–2.84	0.01 ± 0.01	3.04–3.08	0.01 ± 0.01
1.94–2.04	0.03 ± 0.02	2.54–2.64	0.01 ± 0.01	2.84–2.88	0.01 ± 0.02	3.08–3.10	0.27 ± 0.09
2.04–2.14	0.03 ± 0.01	2.64–2.68	0.01 ± 0.01	2.88–2.92	0.01 ± 0.01	3.10–3.12	0.30 ± 0.09
2.14–2.24	0.00 ± 0.01	2.68–2.72	0.01 ± 0.02	2.92–2.96	0.02 ± 0.02	3.12–3.14	0.11 ± 0.05

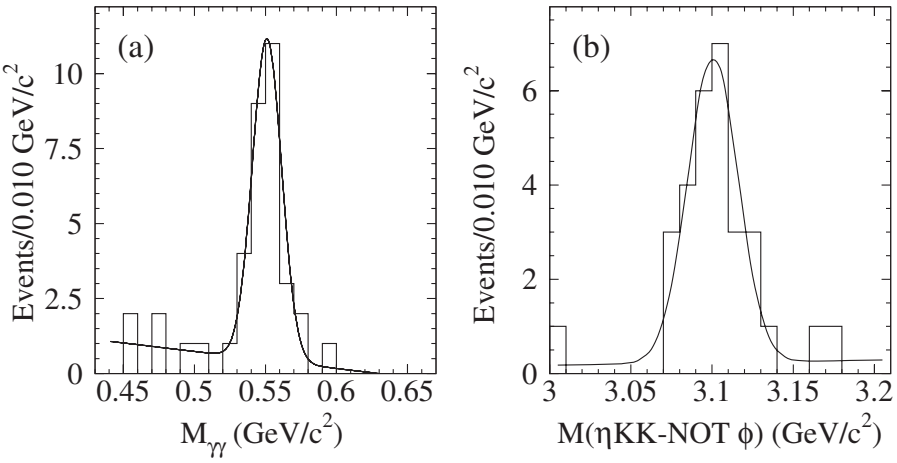

FIG. 31. (a) The $\gamma\gamma$ invariant mass distribution in the η region, when a $J/\psi \to K^+K^-\eta$ decay is selected. (b) The final J/ψ signal ($0.513 < M_{\gamma\gamma} < 0.583$ GeV$/c^2$ required).

similar to those of the $K^+K^-\pi^0$ reaction (see Table IV). However, the background level is so low for the $\phi\eta$ final state that the associated errors are negligible and do not affect the background-subtraction procedures. The systematic uncertainty associated with η reconstruction is equivalent to that for photon reconstruction, and the uncertainty on the $\phi \to K^+K^-$ decay rate is 1.2%. The total systematic error is thus $\pm 5.3\%$, while the efficiency is overestimated by 4.6%. The detection efficiency shown in Fig. 34 as a function of c.m. energy is obtained from MC and accounts also for $\eta \to \gamma\gamma$ decay rate. The corresponding values for the $e^+e^- \to \phi\eta$ cross section, obtained with an expression analogous to Eq. (8), are reported in Table XIV and in Fig. 35.

The cross section peaks at about 3.0 nb around 1.7 GeV and also hints at a possible resonant behavior around 2.1 GeV. Above the J/ψ mass the cross section becomes negligible.

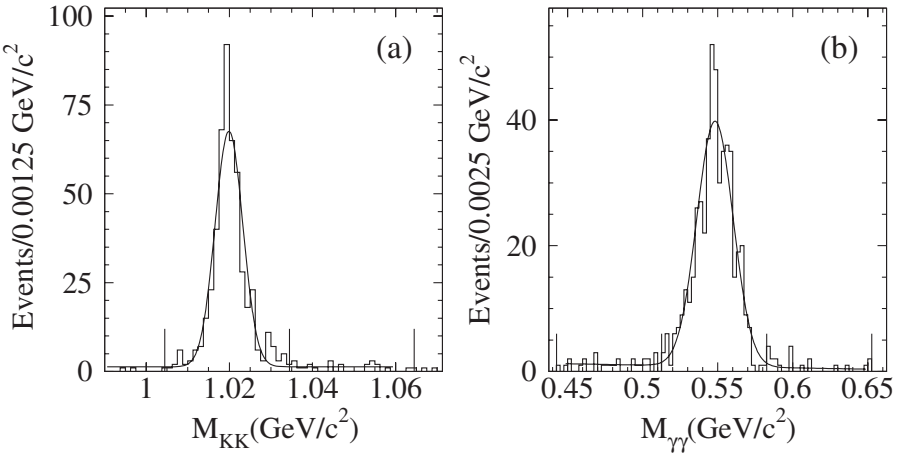

FIG. 32. The K^+K^- (a) and $\gamma\gamma$ (b) invariant mass distributions. Signal and sideband regions are set by vertical lines in the plots.

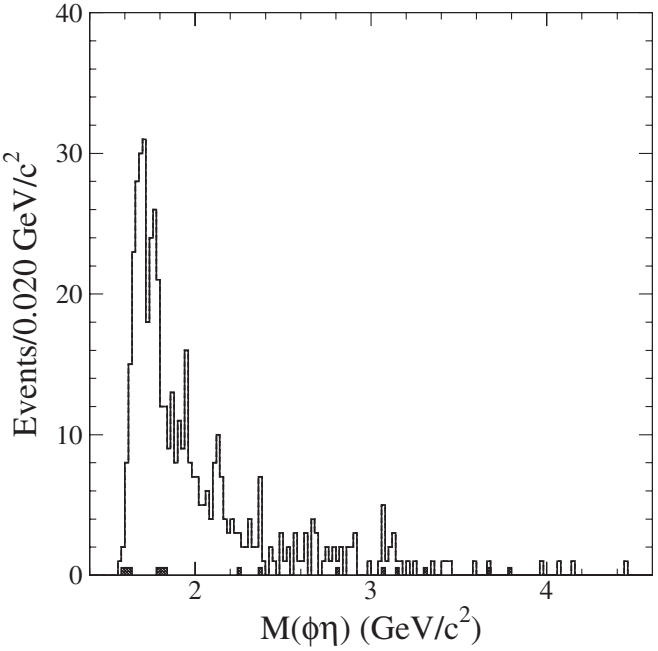

FIG. 33. The invariant mass distribution of the $\phi\eta$ system. The shaded histogram refers to the small subtracted background component.

X. CROSS SECTION FITS

The cross section parametrization used to fit the data leading to the final state f, $e^+e^- \to f$, at $s = E^2_{\rm c.m.}$ is

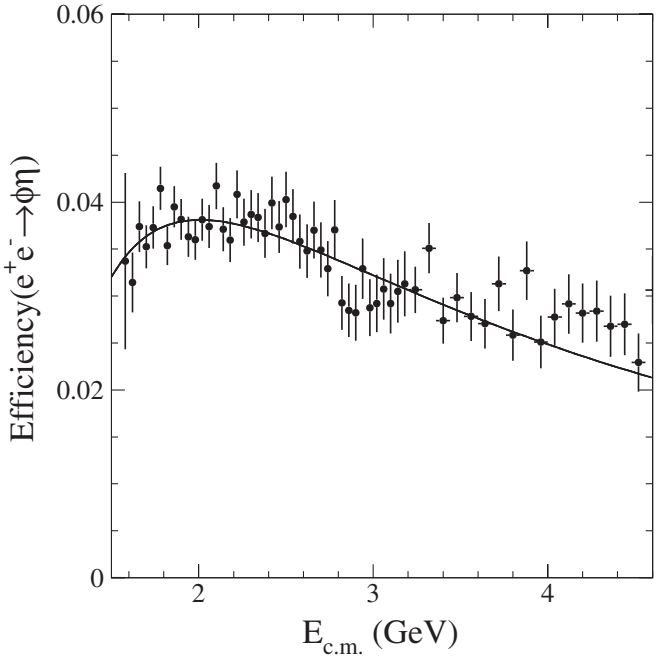

FIG. 34. Detection and reconstruction efficiency as a function of the c.m. energy for the $\phi\eta$ final state. The solid line is the result of a fit to the data with the function $a(1-(x/b)^p \cdot e^{\xi(b-x)})$, where $x = E_{\rm c.m.}$.

$$\sigma_f(s) = 12\pi\mathcal{P}_f(s)\left|A_f^{\rm n.r.}(s) + \sum_R \sqrt{\mathcal{B}_f^R\Gamma_{ee}^R}\frac{\sqrt{\Gamma_R/\mathcal{P}_f(M_R^2)}e^{i\Psi_R}}{M_R^2 - s - i\sqrt{s}\Gamma_R(s)}\right|^2, \quad (11)$$

where $\mathcal{P}_f(s)$ is the phase space of the f final state, $A_f^{\rm n.r.}(s)$ describes the nonresonant background, mainly due to the tails of resonances below threshold, and the sum runs over all the vector resonances, with mass M_R, width Γ_R, and relative phase Ψ_R, assumed to contribute to the cross section. All of the final states analyzed contain a vector and a pseudoscalar meson. The phase space for $f = VP$ has the form:

$$\mathcal{P}_{VP}(s) = \left[\frac{(s + M_V^2 - M_P^2)^2 - 4M_V^2 s}{s}\right]^{3/2}. \quad (12)$$

A. Fitting $K\bar{K}\pi$ and $\phi\eta$ cross sections

The statistics are large enough to attempt a complete description of the $KK^*(892)$ channel. The $K^0_S K^\pm\pi^\mp$ Dalitz plot yields not only the isoscalar σ_0 and isovector σ_1 components, but also their relative phase $\Delta\phi$ (Figs. 16–18). In addition, the $e^+e^- \to K^\pm K^{*\mp}(892)$ cross section, obtained by integrating the $K^+K^-\pi^0$ Dalitz plot multiplied by the isospin factor of 3, and taking into account corrections due to the interference relevant for $K^\pm\pi^0$ in the $K^*(892)$ region, provides a further constraint on σ_0, σ_1, and $\Delta\phi$. Indeed, both the cross sections for $e^+e^- \to K^\pm K^{*\mp}(892)$ and $e^+e^- \to K^0\bar{K}^{*0}(892)$ + c.c. can be defined in terms of opposite combinations of the same isospin components:

$$\begin{aligned}\sigma_{K^0\bar{K}^{*0}(892)+{\rm c.c}} &= |\sqrt{\sigma_0} + \sqrt{\sigma_1}e^{i\Delta\phi}|^2 \\ &= \sigma_0 + \sigma_1 + 2\sqrt{\sigma_0\sigma_1}\cos\Delta\phi, \\ \sigma_{K^\pm K^{*\mp}(892)} &= |\sqrt{\sigma_0} - \sqrt{\sigma_1}e^{i\Delta\phi}|^2 \\ &= \sigma_0 + \sigma_1 - 2\sqrt{\sigma_0\sigma_1}\cos\Delta\phi.\end{aligned} \quad (13)$$

We note that the square root of the cross sections σ_0 and σ_1, having roughly the same phase space (the mass difference between neutral and charged $K^*(892)$ can be neglected here and in the following), are proportional to the corresponding amplitudes. The isoscalar $KK^*(892)$ cross section σ_0 and $\sigma_{\phi\eta}$ appear to be dominated by the same structure, a broad peak with $M \approx 1.7$ GeV/c^2. This behavior is theoretically expected because the two final states have the same quantum numbers $I^G(J^{PC}) = 0^-(1^{--})$ and similar strangeness content. In principle, quantum number conservation should allow ω-like and ϕ-like contributions for both cross sections. However, in the case of the $\phi\eta$ final state, the Okubo-Zweig-Iizuka (OZI) rule [23] strongly suppresses any intermediate ω-recurrence. On the other hand, for the channel $KK^*(892)$, where the OZI rule does not apply, there are also suppression factors.

TABLE XIV. Measurement of the $e^+e^- \to \phi\eta$ cross section as a function of $E_{\rm c.m.}$. Errors are statistical only.

$E_{\rm c.m.}$ (GeV)	σ (nb)	$E_{\rm c.m.}$ (GeV)	σ (nb)	$E_{\rm c.m.}$ (GeV)	σ (nb)	$E_{\rm c.m.}$ (GeV)	σ (nb)
1.56–1.58	0.11 ± 0.11	1.88–1.90	0.64 ± 0.23	2.20–2.22	0.27 ± 0.13	2.64–2.68	0.12 ± 0.06
1.58–1.60	0.16 ± 0.18	1.90–1.92	0.87 ± 0.26	2.22–2.24	0.20 ± 0.12	2.68–2.72	0.09 ± 0.05
1.60–1.62	0.80 ± 0.31	1.92–1.94	0.71 ± 0.24	2.24–2.26	0.16 ± 0.12	2.72–2.76	0.09 ± 0.05
1.62–1.64	1.51 ± 0.41	1.94–1.96	1.24 ± 0.31	2.26–2.28	0.13 ± 0.09	2.76–2.80	0.08 ± 0.05
1.64–1.66	2.34 ± 0.49	1.96–1.98	0.61 ± 0.22	2.28–2.30	0.13 ± 0.09	2.80–2.84	0.07 ± 0.05
1.66–1.68	2.78 ± 0.53	1.98–2.00	0.53 ± 0.20	2.30–2.32	0.26 ± 0.13	2.84–2.88	0.06 ± 0.04
1.68–1.70	2.91 ± 0.53	2.00–2.02	0.52 ± 0.20	2.32–2.34	0.13 ± 0.09	2.88–2.94	0.09 ± 0.04
1.70–1.72	2.94 ± 0.53	2.02–2.04	0.37 ± 0.16	2.34–2.36	0.13 ± 0.09	2.94–3.00	0.02 ± 0.02
1.72–1.74	1.67 ± 0.39	2.04–2.06	0.36 ± 0.16	2.36–2.38	0.41 ± 0.17	3.00–3.06	0.02 ± 0.02
1.74–1.76	2.18 ± 0.45	2.06–2.08	0.43 ± 0.18	2.38–2.40	0.06 ± 0.06	3.06–3.12	0.13 ± 0.05
1.76–1.78	2.32 ± 0.45	2.08–2.10	0.29 ± 0.14	2.40–2.44	0.06 ± 0.04	3.12–3.18	0.08 ± 0.04
1.78–1.80	1.79 ± 0.41	2.10–2.12	0.56 ± 0.20	2.44–2.48	0.03 ± 0.03	3.18–3.24	0.02 ± 0.02
1.80–1.82	0.99 ± 0.30	2.12–2.14	0.70 ± 0.22	2.48–2.52	0.12 ± 0.06	3.24–3.30	0.02 ± 0.02
1.82–1.84	0.97 ± 0.30	2.14–2.16	0.48 ± 0.18	2.52–2.56	0.06 ± 0.04	3.30–3.36	0.01 ± 0.02
1.84–1.86	0.75 ± 0.25	2.16–2.18	0.27 ± 0.14	2.56–2.60	0.12 ± 0.06	3.36–3.42	0.02 ± 0.02
1.86–1.88	1.06 ± 0.30	2.18–2.20	0.20 ± 0.12	2.60–2.64	0.12 ± 0.06	3.42–3.48	0.03 ± 0.02

Suppression of ω-like versus ϕ-like coupling could account for as much as a factor of 4 [17,24]; an additional price has to be paid if a strange quark pair has to be created from the vacuum. Hence, in the following we will consider all the structures contributing to the isoscalar amplitudes as ϕ-like resonances. In particular, the peak with $M \approx 1.7\ \mathrm{GeV}/c^2$ matches the first ϕ-like excited state, so we will assume it to be simply the ϕ'.

The first result that can be drawn comparing the cross section data on σ_0 and $\sigma_{\phi\eta}$ (Figs. 16 and 35) is an estimate for the ratio between the decay fractions of the ϕ' into

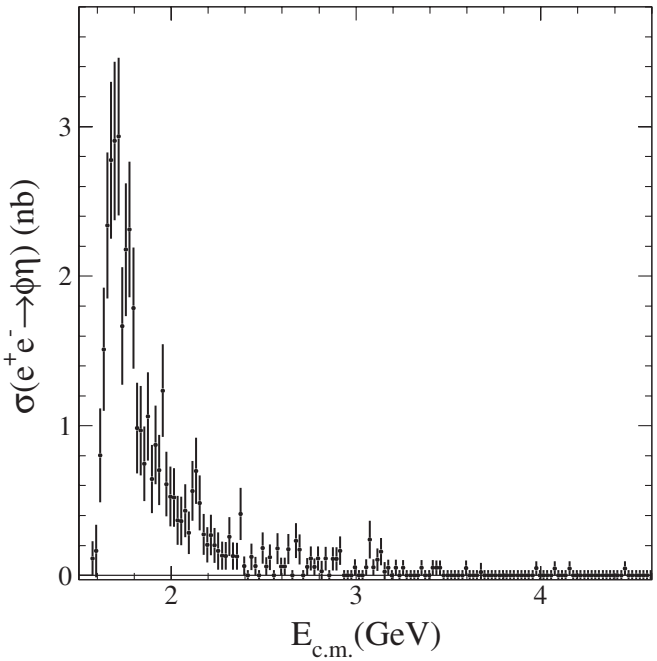

FIG. 35. The $e^+e^- \to \phi\eta$ cross section distribution as a function of c.m. energy.

$KK^*(892)$ and $\phi\eta$. Indeed, at the ϕ' peak:

$$\frac{\sigma_{\phi\eta}(M^2_{\phi'})}{\sigma_0(M^2_{\phi'})} \approx \frac{\mathcal{B}^{\phi'}_{\phi\eta}}{\mathcal{B}^{\phi'}_{KK^*(892)}} \approx \frac{1}{3}, \tag{14}$$

where $\mathcal{B}^R_f$ is the branching ratio for the decay $R \to f$. From Eq. (14) one can infer that both the $KK^*(892)$ and the $\phi\eta$ channel represent an important fraction of the ϕ' total width.

In order to make optimal use of the experimental data, we perform a global fit exploiting all available information from the $K\bar{K}\pi$ final states (four sets of data: σ_0, σ_1, $\Delta\phi$, and $\sigma_{K^\pm K^{*\mp}(892)}$) as well as the $\phi\eta$ cross section.

We have considered also a recently published *BABAR* measurement on the $\phi\eta$ cross section [25] in the $e^+e^- \to K^+K^-\pi^+\pi^-\pi^0$ channel. These data, even though with a lower statistics, are in agreement with our measurement.

We have performed two fits, in the first case we used only our samples (five sets of data: σ_0, σ_1, $\Delta\phi$, $\sigma_{K^\pm K^{*\mp}(892)}$, and $\sigma_{\phi\eta}$), in the second case we included the $\phi\eta$ cross section from Ref. [25].

We parametrize the $K\bar{K}\pi$ isoscalar and the isovector cross sections using Eq. (11) with one resonance each and a nonresonant background, assumed to be the ϕ tail. The isoscalar cross section shows a clearly resonant behavior, the shape of the subdominant isovector cross section instead appears compatible with a pure phase space. However, using the information of the relative phase, $\Delta\phi$ (Fig. 18), it can be shown that such a quantity is not consistent with a real isovector amplitude, as expected in the case of a nonresonant behavior. If this were indeed the case, the relative phase should be as shown by the light-gray band in Fig. 36. This is clearly not compatible with the data (solid circles). The isovector cross section σ_1, then,

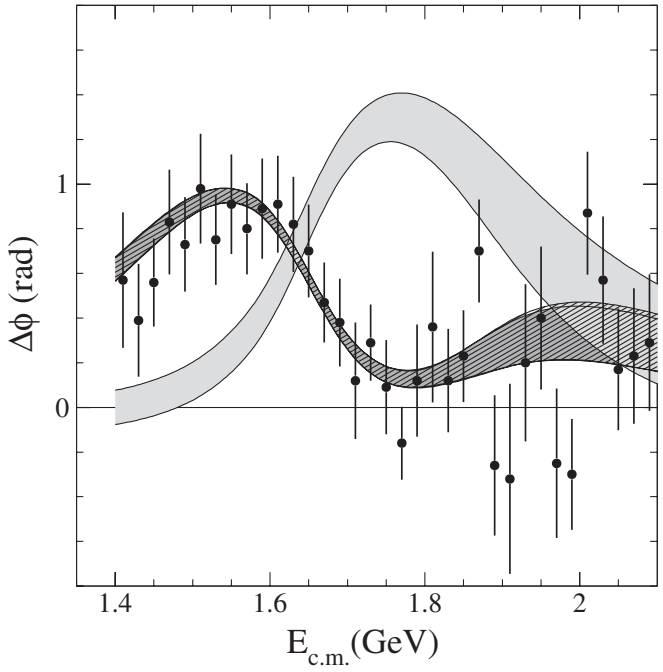

FIG. 36. Phase difference between isovector and isoscalar $KK^*(892)$ amplitudes: data and fits superimposed (dark-gray and hatched bands). In particular the dark-gray band is obtained by using only our $\phi\eta$ cross section, while the hatched band includes also the data from Ref. [25]. The light-gray band represents the relative phase expected in case of nonresonant isovector component.

has to be described in terms of a ρ-like excited state, the ρ' in the following.

Finally, the $\phi\eta$ cross section is parametrized using two resonances: in addition to the dominant ϕ' just above threshold, we include a small contribution, probably due to an excited $s\bar{s}$ or a more exotic state (tetraquark, hybrid) with a mass around 2.13 GeV/c^2, the ϕ'', that has been observed decaying into $\phi f_0(980)$ [26].

A good parametrization of the nonresonant background, the function $A_f^{\text{n.r.}}(s)$ ($f = KK^*(892), \phi\eta$), can be obtained using a $1/s$ scaling ($A_f^{\text{n.r.}}(s) \equiv A_f^{\text{n.r.}}/s$). As a result, the shape of the nonresonant part, Eq. (11), is essentially given by the phase space, and we may define the nonresonant cross section as

$$\sigma_f^{\text{bkg}}(s) = 12\pi\mathcal{P}_f(s)[A_f^{\text{n.r.}}/s]^2. \tag{15}$$

We stress that, as shown in Table XV, this cross section represents only a small fraction of the resonant one.

We describe wide resonances using energy-dependent widths, $\Gamma_R(s)$ [see Eq. (11)], parametrized as

$$\Gamma_R(s) = \Gamma_R \sum_k \frac{\mathcal{P}_k(s)}{\mathcal{P}_k(M_R^2)} \mathcal{B}_k^R, \tag{16}$$

where Γ_R is the constant total width, and $\mathcal{P}_k(s)$ and $\mathcal{B}_k^R$ are the phase space and the branching fraction for the transition of R into the final state k, respectively ($\sum_k \mathcal{B}_k^R = 1$). In case of narrow peaks we use fixed widths.

As already mentioned, the most important resonance in these processes is the ϕ': it represents the main contribution for both σ_0 and $\sigma_{\phi\eta}$. It follows that the total width $\Gamma_{\phi'}(s)$ will account for both these VP-like final states: the isoscalar $KK^*(892)$ and the $\phi\eta$. Other final states with small branching ratios are parametrized by adding a constant term to the width

TABLE XV. Parameters for resonances ϕ' and ρ' obtained by fitting simultaneously the isoscalar and isovector component of the $K\bar{K}^*(892)$ + c.c. cross section, their relative phase, the $K^+K^-\pi^0$ and the $\phi\eta$ cross sections (only our samples on the left, including also data from Ref. [25] on the right). Real backgrounds are defined through Eq. (15). All phases Ψ_R [see Eq. (11)] are set to zero.

	$\frac{\chi^2}{\text{n.d.f.}} = \frac{184.9}{160-16} = 1.28$		$\frac{\chi^2}{\text{n.d.f.}} = \frac{205.4}{187-16} = 1.20$	
R with $I = 0$	ϕ'	ϕ''	ϕ'	ϕ''
$\Gamma_{ee}^R \mathcal{B}_{KK^*(892)}^R$ (eV)	367 ± 47	—	369 ± 53	—
$\Gamma_{ee}^R \mathcal{B}_{\phi\eta}^R$ (eV)	154 ± 32	1.7 ± 0.8	138 ± 33	1.7 ± 0.7
$1 - \mathcal{B}_{KK^*(892)}^R - \mathcal{B}_{\phi\eta}^R$	0.33 ± 0.14	—	0.36 ± 0.15	—
M_R (MeV)	1709 ± 19	2127 ± 24	1709 ± 20	2125 ± 22
Γ_R (MeV)	325 ± 68	60 ± 50	322 ± 77	61 ± 50
$\sigma_{KK^*(892)}^{\text{bkg}}(M_{\phi'}^2)$ (nb)	0.8 ± 0.3	—	0.9 ± 0.3	—
$\sigma_{\phi\eta}^{\text{bkg}}(M_{\phi'}^2)$ (nb)	$(4.7 \pm 1.4) \times 10^{-3}$		$(4.7 \pm 1.8) \times 10^{-3}$	

R with $I = 1$	ρ'	ρ'
$\Gamma_{ee}^R \mathcal{B}_{KK^*(892)}^R$ (eV)	129 ± 15	127 ± 15
$1 - \mathcal{B}_{4\pi}^R$	0.36 ± 0.22	0.35 ± 0.23
M_R (MeV)	1508 ± 19	1505 ± 19
Γ_R (MeV)	418 ± 26	418 ± 25
$\sigma_{KK^*(892)}^{\text{bkg}}(M_{\rho'}^2)$ (nb)	0.9 ± 0.2	0.9 ± 0.2

$$\Gamma_{\phi'}(s) = \Gamma_{\phi'}\Big[\frac{\mathcal{P}_{KK^*(892)}(s)}{\mathcal{P}_{KK^*(892)}(M^2_{\phi'})}\mathcal{B}^{\phi'}_{KK^*(892)} + \frac{\mathcal{P}_{\phi\eta}(s)}{\mathcal{P}_{\phi\eta}(M^2_{\phi'})}\mathcal{B}^{\phi'}_{\phi\eta} + (1 - \mathcal{B}^{\phi'}_{KK^*(892)} - \mathcal{B}^{\phi'}_{\phi\eta})\Big]. \quad (17)$$

The ϕ'', with a constant width, is included to model the $\phi\eta$ cross section.

The main contribution to the cross section σ_1 comes from the ρ' resonance. We assume the ρ' to decay mainly in four pions, and again include a constant term to account for other channels:

$$\Gamma_{\rho'}(s) = \Gamma_{\rho'}\Big[\frac{\mathcal{P}_{4\pi}(s)}{\mathcal{P}_{4\pi}(M^2_{\rho'})}\mathcal{B}^{\rho'}_{4\pi} + (1 - \mathcal{B}^{\rho'}_{4\pi})\Big], \quad (18)$$

where, for $\mathcal{P}_{4\pi}(s)$ we use

$$\mathcal{P}_{4\pi}(s) = \frac{(s - 16M^2_\pi)^n}{s}, \quad (19)$$

with $n = 3/2$. Note that the fit is not sensitive to this power, as higher values (e.g. $n = 5/2$) give similar parameters.

Our global-fit results are summarized in Table XV and shown in Figs. 36–39, where the errors of data points include both statistical and systematic uncertainties, and the bands represent the convolution of the one-sigma statistical errors of the fit. The solid and the hatched fill refer to the two considered cases. In particular, Figs. 36 and 37 show data and fits for the isospin components and the relative phase from the $K^0_S K^\pm\pi^\mp$ Dalitz plot analysis, Fig. 38 shows the cross section $\sigma_{K^\pm K^{*\mp}(892)}$, and Fig. 39 shows $\sigma_{\phi\eta}$, as obtained in this analysis and in Ref. [25].

All these data sets support the hypothesis that the main contribution in the isoscalar amplitudes is the resonance ϕ', while the isovector component is almost fully described by a broad excited ρ state. However, the normalized $\frac{\chi^2}{\text{n.d.f.}}$ values, 1.28 in the first case and 1.20 in the second case when the data on the $\phi\eta$ cross section from Ref. [25]

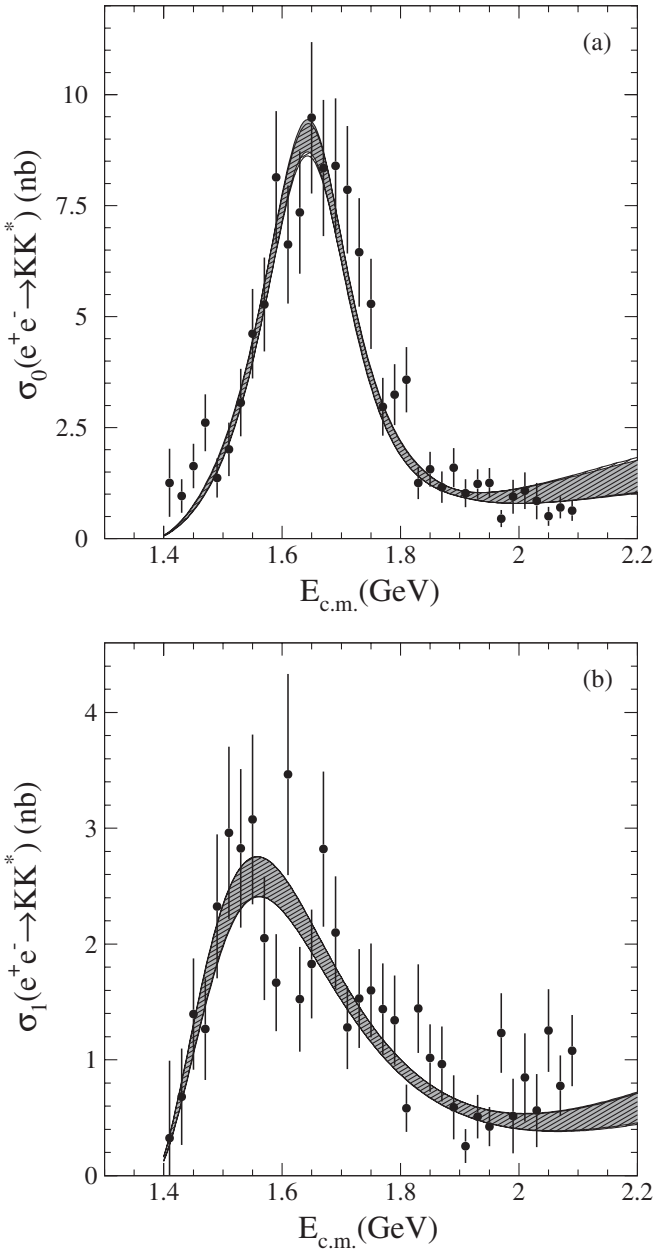

FIG. 37. Isoscalar (a) and isovector (b) components of the $K^0_S K^\pm\pi^\mp$ cross section. The solid points are the data and the bands represent the fits. The hatched band is obtained including the $\phi\eta$ cross section from Ref. [25].

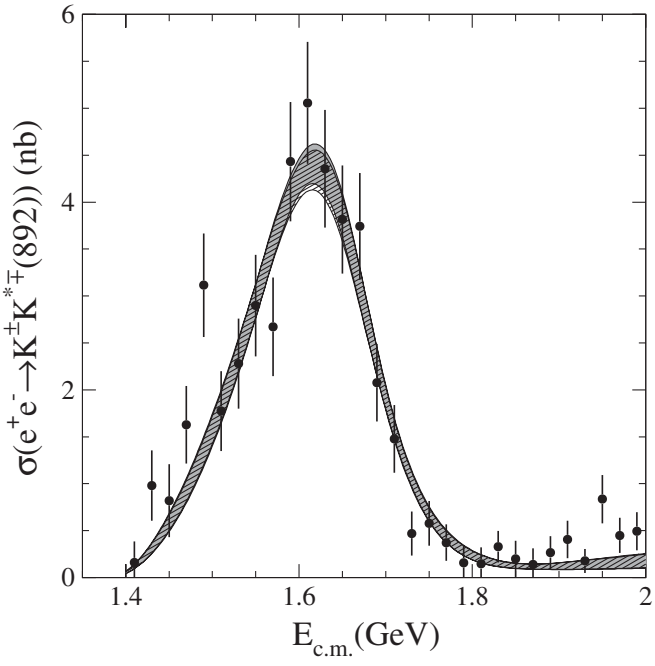

FIG. 38. Data on the annihilation cross section $\sigma_{K^\pm K^{*\mp}(892)}$, see Eq. (13), and descriptions (solid and hatched bands) in terms of the parametrization of Eq. (11), with parameters reported in Table XV. The hatched band is obtained including the $\phi\eta$ cross section from Ref. [25].

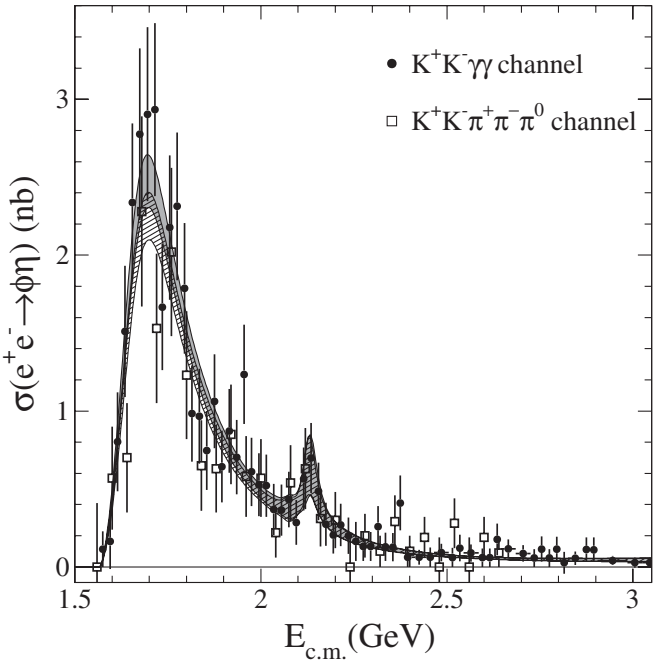

FIG. 39. Data on the annihilation cross section $\sigma_{\phi\eta}$ (the solid circles are from this analysis, while the empty squares are from Ref. [25]) and descriptions (solid and hatched bands) in terms of the parametrization of Eq. (11), with parameters reported in Table XV. The hatched band is obtained including the $\phi\eta$ cross section from Ref. [25].

are used, do not exclude the presence of other possible structures but, on the other hand, the accuracy of the data does not allow any clear identification.

As mentioned above, the mass and width of the ϕ' are compatible with the $\phi(1680)$ [17]. The parameters obtained for the ϕ'', the second isoscalar excited state, are consistent with those reported in Ref. [26]. A clear evidence for this decay channel cannot be established with the available data sample, however, the probability to be a statistical fluctuation is 6×10^{-4} (25 events under the peak with an expectation of 11 evaluated from the mass spectrum in Fig. 35). The ρ' from the isovector component of the $KK^*(892)$ cross section has a mass value in agreement with Ref. [17], although this agreement is not particularly striking given the width of this resonance.

It is worth stressing that at $E_{\rm c.m.}$ above 1.8 GeV, contributions coming from any higher mass K^* certainly affect the fit in the $KK^*(892)$ channel. At low $E_{\rm c.m.}$ the fit is very sensitive to the $K^*(892)$ width, when the $K\pi$ invariant mass is close to the $K^*(892)$ threshold. However, analyticity relates $KK^*(892)$ and $\phi\eta$ amplitudes to the $K^*(892)$ and ϕ radiative widths (that is $KK^*(892)$ and $\phi\eta$ at $s = 0$) via dispersion relations. Exploiting these relations might lead to an improved determination of the threshold cross section.

The systematic effects due to the choice of fit model were evaluated by repeating the fits using different values for the relative phases Ψ_R, and by choosing different parametrizations for the energy-dependent widths, as appropriate.

B. Fitting the $\phi\pi^0$ cross section

The $\phi\pi^0$ channel is a pure isospin one final state, hence, using Eq. (11) to describe the corresponding cross section, only isovector contributions must be included. This channel has been selected as a possible candidate for multiquark intermediate states: contributions are expected from ρ recurrences, even though they are OZI-suppressed. We label any resonance in this channel as a ρ-like excited state.

Two cases have been studied in detail:

(i) only one ρ-like excited state, a ρ'' (to distinguish it from the ρ' of the previous case);

(ii) two ρ recurrences, i.e., in addition to ρ'', a narrow resonance to better represent the data around $E_{\rm c.m.} \approx$ 1900 MeV (Fig. 40), labeled in the following as $\rho(1900)$.

The $\rho(1900)$ width is assumed constant, while for the ρ'' we use the energy-dependent width

$$\Gamma_{\rho''}(s) = \Gamma_{\rho''}\left[\frac{\mathcal{P}_{4\pi}(s)}{\mathcal{P}_{4\pi}(M^2_{\rho''})}\mathcal{B}^{\rho''}_{4\pi} + (1 - \mathcal{B}^{\rho''}_{4\pi})\right],$$

where $\mathcal{P}_{4\pi}(s)$ is the four-pion phase space defined in Eq. (19), and $\mathcal{B}^{\rho''}_{4\pi}$ is the branching fraction for $\rho'' \to 4\pi$.

The results of the fit with only the ρ'' are reported in the first column of Table XVI.

In the second case, where the $\rho(1900)$ is also included, a two step procedure is used to determine the phases of the

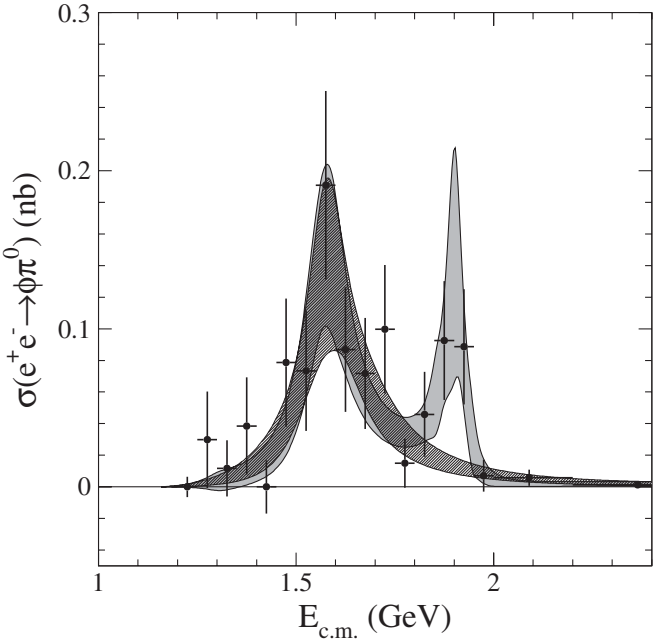

FIG. 40. Data on the annihilation cross section $\sigma_{\phi\pi^0}$ and descriptions in terms of the parametrization of Eq. (11) with the only ρ'', hatched band, and including also the $\rho(1900)$, gray band.

TABLE XVI. Parameters obtained for the $\phi\pi^0$ cross section. First column: with the only ρ'' resonance, second and third columns: including also the $\rho(1900)$. The normalized χ^2 and corresponding C.L. are reported in each case.

$(\frac{\chi^2}{\text{n.d.f.}}, \text{C.L.})$	$(\frac{14.36}{16-5}, 0.31)$	$(\frac{7.37}{16-8}, 0.50)$	
R	ρ''	ρ''	$\rho(1900)$
$\Gamma^R_{ee}\mathcal{B}^R_{\phi\pi^0}$ (eV)	4.4 ± 1.0	3.5 ± 0.9	2.0 ± 0.6
$(1 - \mathcal{B}^R_{4\pi})$	0.67 ± 0.43	0.44 ± 0.49	—
M_R (MeV)	1593 ± 32	1570 ± 36	1909 ± 17
Γ_R (MeV)	203 ± 97	144 ± 75	48 ± 17
Ψ_R (rad)	0	0	π
$\sigma^{\text{bkg}}_{\phi\pi^0}(M^2_{\rho(1900)})$ (nb)	$(0.4 \pm 0.2) \times 10^{-3}$	$(0.5 \pm 1.5) \times 10^{-3}$	

two quasireal amplitudes. We find $(\Psi_{\rho''}, \Psi_{\rho(1900)}) = (0, \pi)$ to be the best combination. With these phases we get the results reported in the second and third columns of Table XVI.

The results of the two fits are shown in Fig. 40, superimposed on the cross section data.

A slightly better χ^2 is obtained by adding this extra resonance. We cannot, however, exclude that the observed accumulation of events at $E_{\text{c.m.}} \approx 1.9$ GeV is produced by a statistical fluctuation. In fact, we observe 18 events to be compared to an expectation of 8 events, taking into account both the background and the tail of the ρ'', and this translates in a Poisson probability of 2×10^{-3}.

Mass, width, and quantum numbers $[I^G(J^{PC}) = 1^+(1^{--})]$ obtained for the $\rho(1900)$ are compatible with those of the so-called "dip" observed in other channels, primarily multipion final states [27].

XI. SUMMARY AND CONCLUSIONS

We have studied the $K^0_S K^\pm\pi^\mp$, $K^+K^-\pi^0$, $\phi\pi^0$, $K^+K^-\eta$, and $\phi\eta$ final states, produced in *BABAR* via ISR.

We have measured the production cross section from threshold up to ≈ 4.6 GeV for all of these processes to an unprecedented accuracy.

By studying the asymmetric $K^0_S K^\pm\pi^\mp$ Dalitz plot, we have obtained the moduli and relative phase of the isospin components for the $KK^*(892)$ cross section. The knowledge of the isoscalar and isovector cross sections, σ_0 and σ_1, allows a simple description in terms of vector meson resonances, where ρ- and ϕ-like mesons do not mix. In addition, the relative phase gives unique information on the subdominant isovector component, which, although compatible with a pure phase space behavior, reveals a resonant structure.

Two global fits that benefit from five interconnected sources of information (σ_0, σ_1, $\sigma_{\phi\eta}$, $\sigma_{K^+K^-\pi^0}$, and $\Delta\phi$) have been performed. In the first case we have used only the data samples coming from this analysis, while in the second case recent *BABAR* data on $\sigma_{\phi\eta}$ in the $K^+K^-\pi^+\pi^-\pi^0$ channel have been included.

Both $\phi\eta$ and the isoscalar $KK^*(892)$ cross sections have been parametrized with the same dominant resonance ϕ'; the suitable combination of σ_0, σ_1, and $\Delta\phi$, obtained from the $K^0_S K^\pm\pi^\mp$ channel, is used to describe the $K^+K^-\pi^0$ cross section. The mass and width for the ϕ', the main resonant contribution in the isoscalar channels, are compatible with those of the $\phi(1680)$ meson reported in Ref. [17]. Concerning the ϕ'' resonance, included only in the $\phi\eta$ channel, we find parameters compatible with those of the first observation in the $\phi f_0(980)$ final state [26], confirming the quantum numbers of this resonance, $I^G(J^{PC}) = 0^-(1^{--})$.

The isovector component of the $KK^*(892)$ cross section is described by one broad resonance, ρ', whose mass is compatible with the $\rho(1450)$, the first ρ recurrence. The slight inconsistency for the width is probably due to the fact that a single structure is not sufficient to describe this cross section and that the fit tends to broaden the ρ' to mimic a more complex structure. The present statistics does not allow the identification of multiple structures.

The $\phi\pi^0$ cross section has been fit with ρ recurrences, whose coupling with the final state is, however, OZI-suppressed. Two possible descriptions have been considered, with one and two resonances. Their parameters are reported in Table XVI.

The resonance labeled ρ'' might be the so-called $C(1480)$ observed in $\pi^- p \to \phi\pi^0 n$ charge-exchange reactions [28] in the same $\phi\pi^0$ final state. However, a firm conclusion cannot be drawn at the moment; an OZI-violating decay of the meson $\rho(1700)$ [17] cannot be excluded. The second structure, $\rho(1900)$, is compatible with the dip already observed in other experiments, predominantly in multipion final states [27].

In Table XVII we summarize the whole set of parameters obtained from the fit to the cross sections, with the inclusion of model related systematic errors.

As already pointed out, the normalized χ^2's obtained from this global-fit procedure are still compatible with other possible minor contributions that, however, cannot be precisely identified because of the accuracy of the data.

In the (2–3) GeV c.m. energy region the $K^0_S K^\pm\pi^\mp$ final state has been analyzed, adding the $K^*_2(1430)K$ to the $K^*(892)K$ intermediate state. The strong asymmetry between neutral and charged channels of the Dalitz plot ($M^2_{K_S\pi^\pm}$ vs $M^2_{K^\pm\pi^\mp}$) can be explained in terms of construc-

TABLE XVII. Summary of parameters of resonances in the studied final states, obtained including also the data on the $\phi\eta$ cross section from Ref. [25]. The parameters for the ρ'' are taken from the fit to the $\phi\pi^0$ cross section with two resonances.

Isospin	R	$\Gamma^R_{ee}\mathcal{B}^R_{KK^*(892)}$ (eV)	$\Gamma^R_{ee}\mathcal{B}^R_{\phi\eta}$ (eV)	M_R (MeV)	Γ_R (MeV)
0	ϕ'	$369 \pm 53 \pm 1$	$138 \pm 33 \pm 28$	$1709 \pm 20 \pm 43$	$322 \pm 77 \pm 160$
	ϕ''	—	$1.7 \pm 0.7 \pm 1.3$	$2125 \pm 22 \pm 10$	$61 \pm 50 \pm 13$

Isospin	R	$\Gamma^R_{ee}\mathcal{B}^R_{KK^*(892)}$ (eV)	$\Gamma^R_{ee}\mathcal{B}^R_{\phi\pi^0}$ (eV)	M_R (MeV))	Γ_R (MeV)
1	ρ'	$127 \pm 15 \pm 6$	—	$1505 \pm 19 \pm 7$	$418 \pm 25 \pm 4$
	ρ''	—	$3.5 \pm 0.9 \pm 0.3$	$1570 \pm 36 \pm 62$	$144 \pm 75 \pm 43$
	$\rho(1900)$	—	$2.0 \pm 0.6 \pm 0.4$	$1909 \pm 17 \pm 25$	$48 \pm 17 \pm 2$

tive and destructive interference between different isospin components. This asymmetry might be connected to a similar effect observed in the radiative decay rates of the neutral and charged $K_2^*(1430)$ [17].

Very clean J/ψ signals have been observed in most of the studied final states, allowing the measurement of the corresponding branching fractions.

We have no evidence of the $Y(4260)$ decaying into $K^0_S K^\pm \pi^\mp$ and $K^+K^-\pi^0$. We determine $\Gamma^{Y(4260)}_{ee} \times \mathcal{B}^{Y(4260)}_{K^0_S K^\pm \pi^\mp} < 0.5$ eV and $\Gamma^{Y(4260)}_{ee}\mathcal{B}^{Y(4260)}_{K^+K^-\pi^0} < 0.6$ eV at 90% C.L. We observe also (inset of Fig. 6) a 3.5σ fluctuation in the $e^+e^- \to K^0_S K^\pm \pi^\mp$ cross section at $E_{\rm c.m.} \approx 4.20$ GeV.

ACKNOWLEDGMENTS

We warmly acknowledge Stanley Brodsky for very fruitful discussions and suggestions on many aspects of this work. We are grateful for the extraordinary contributions of our PEP-II colleagues in achieving the excellent luminosity and machine conditions that have made this work possible. The success of this project also relies critically on the expertise and dedication of the computing organizations that support *BABAR*. The collaborating institutions wish to thank SLAC for its support and the kind hospitality extended to them. This work is supported by the U.S. Department of Energy and National Science Foundation, the Natural Sciences and Engineering Research Council (Canada), the Commissariat à l'Energie Atomique and Institut National de Physique Nucléaire et de Physique des Particules (France), the Bundesministerium für Bildung und Forschung and Deutsche Forschungsgemeinschaft (Germany), the Istituto Nazionale di Fisica Nucleare (Italy), the Foundation for Fundamental Research on Matter (The Netherlands), the Research Council of Norway, the Ministry of Science and Technology of the Russian Federation, Ministerio de Educación y Ciencia (Spain), and the Science and Technology Facilities Council (United Kingdom). Individuals have received support from the Marie-Curie IEF program (European Union) and the A. P. Sloan Foundation.

[1] B. Aubert *et al.* (*BABAR* Collaboration), Nucl. Instrum. Methods Phys. Res., Sect. A **479**, 1 (2002).
[2] V. N. Baier and V. S. Fadin, Phys. Lett. B **27**, 223 (1968).
[3] A. B. Arbuzov *et al.*, J. High Energy Phys. 12 (1998) 009.
[4] S. Binner, J. H. Kuehn, and K. Melnikov, Phys. Lett. B **459**, 279 (1999).
[5] M. Benayoun *et al.*, Mod. Phys. Lett. A **14**, 2605 (1999).
[6] H. Czyz, A. Grzelinska, J. H. Kuhn, and G. Rodrigo, Eur. Phys. J. C **33**, 333 (2004).
[7] H. Czyz and J. H. Kuhn, Eur. Phys. J. C **18**, 497 (2001); H. Czyz, A. Grzelinska, J. H. Kuhn, and G. Rodrigo, Eur. Phys. J. C **47**, 617 (2006).
[8] A. B. Arbuzov *et al.*, J. High Energy Phys. 10 (1997) 001.
[9] M. Caffo, H. Czyz, and E. Remiddi, Nuovo Cimento Soc. Ital. Fis. A **110**, 515 (1997); Phys. Lett. B **327**, 369 (1994).
[10] E. Barberio, B. van Eijk, and Z. Was, Comput. Phys. Commun. **66**, 115 (1991).
[11] T. Sjostrand, Comput. Phys. Commun. **82**, 74 (1994).
[12] S. Jadach and Z. Was, Comput. Phys. Commun. **85**, 453 (1995).
[13] S. Agostinelli *et al.* (GEANT4 Collaboration), Nucl. Instrum. Methods Phys. Res., Sect. A **506**, 250 (2003).
[14] B. Aubert *et al.* (*BABAR* Collaboration), Phys. Rev. D **71**, 052001 (2005).
[15] B. Aubert *et al.* (*BABAR* Collaboration), Phys. Rev. D **76**, 012008 (2007).
[16] B. Aubert *et al.* (*BABAR* Collaboration), Phys. Rev. D **73**, 052003 (2006).
[17] W. M. Yao *et al.*, J. Phys. G **33**, 1 (2006).
[18] B. Aubert *et al.* (*BABAR* Collaboration), Phys. Rev. Lett. **95**, 142001 (2005).
[19] J. Buon *et al.*, Phys. Lett. B **118**, 221 (1982); D. Bisello *et al.* (Particle and Fields), Z. Phys. C **52**, 227 (1991).
[20] C. Dionisi *et al.*, Nucl. Phys. **B169**, 1 (1980).
[21] C. Zemach, Phys. Rev. **140**, B97 (1965).
[22] D. Carlsmith *et al.*, Phys. Rev. D **36**, 3502 (1987).

[23] S. Okubo, Phys. Lett. **5**, 165 (1963); G. Zweig, CERN Report No. S419/TH412 1964 (unpublished); I. Iizuka, K. Okada, and O. Shito, Prog. Theor. Phys. **35**, 1061 (1966).
[24] N. N. Achasov and A. A. Kozhevnikov, Phys. Rev. D **57**, 4334 (1998).
[25] B. Aubert *et al.* (*BABAR* Collaboration), Phys. Rev. D **76**, 092005 (2007).
[26] B. Aubert *et al.* (*BABAR* Collaboration), Phys. Rev. D **74**, 091103 (2006).
[27] R. Baldini *et al.*, "FENICE" workshop, Frascati (1998); P. L. Frabetti *et al.*, Phys. Lett. B **514**, 240 (2001); P. L. Frabetti *et al.*, Phys. Lett. B **578**, 290 (2004); B. Aubert *et al.* (*BABAR* Collaboration), Phys. Rev. D **73**, 052003 (2006).
[28] S. I. Bityukov *et al.*, Phys. Lett. B **188**, 383 (1987).